Diploma thesis

# PIV measurements of overflow over embankments with different permeabilities

Submitted in satisfaction of the requirements for the degree of
Diplom-Ingenieurin
of the TU Wien, Faculty of Civil Engineering

---

DIPLOMARBEIT

# PIV-Messungen des Überlaufs über Dämme mit unterschiedlichen Durchlässigkeiten

ausgeführt zum Zwecke der Erlangung des akademischen Grades eines / einer
Diplom-Ingenieurin
eingereicht an der Technischen Universität Wien, Fakultät für Bauingenieurwesen

von

**Antonia Treykorn,** BSc

Matr.Nr.: 12104924

unter der Anleitung von

Univ.Ass. Dr.sc. **Gauthier Paul Daniel Marie Rousseau**

Univ.Prof. ir. PhD **Koen Blanckaert**

Institut für Wasserbau und Ingenieurhydrologie
Forschungsbereich Wassebau
Technische Universität Wien,
Karlsplatz 13/E222-1, A-1040 Wien

Wien, November 2024 [redacted]

TECHNISCHE
UNIVERSITÄT
WIEN
Vienna University of Technology

Ich habe zur Kenntnis genommen, dass ich zur Drucklegung meiner Arbeit unter der Bezeichnung

**DIPLOMARBEIT**

nur mit Bewilligung der Prüfungskommission berechtigt bin.

Ich erkläre weiters an Eides statt, dass ich meine Diplomarbeit nach den anerkannten Grundsätzen für wissenschaftliche Abhandlungen selbständig ausgeführt habe und alle verwendeten Hilfsmittel, insbesondere die zugrunde gelegte Literatur genannt habe.

02.12.2024
Datum

[redacted]
Unterschrift

**Abstract**

Embankments play a vital role in flood defense, power generation, and infrastructure. When they fail, particularly in flood-prone regions, the consequences can be severe. Earthen embankments are particularly susceptible to failures from overtopping, seepage, and internal erosion, which are expected to become more common due to shifts in precipitation patterns linked to climate change. To predict and understand embankment stability, both seepage and overflow processes must be analyzed numerically together, as their combined effect can differ from assessing them individually.

The Lattice-Boltzmann Method offers a novel approach for modeling interactions between open channel flows and porous structures, enabling precise simulations of phase transitions. Badarch et al. (2020) successfully applied this method to numerically model overflow and seepage through and over embankments.

The aim of the present work is to develop an experimental setup to measure flow velocities over permeable embankments. This includes using embankments with different permeabilities and measuring the velocity using Particle Image Velocimetry. The analysis of the velocity fields shows that the more permeable material (PPI45) on the upstream slope and the embankment crest had higher velocities than the less permeable PPI60. Conversely, PPI60 exhibited higher velocities on the downstream slope, which is to be expected due to the higher water depth. Captured velocity field are expected to be compared with the numerical model developed by Badarch et al. (2020) in a near future.

**Zusammenfassung**

Dämme spielen eine wichtige Rolle für den Hochwasserschutz, die Stromerzeugung und die Infrastruktur. Ihr Versagen, besonders in hochwassergefährdeten Regionen, kann schwerwiegende Folgen haben. Erddämme sind besonders anfällig für Versagen durch Überströmen, Sickerwasser und innere Erosion, die aufgrund der veränderten Niederschlagsverhältnisse im Zusammenhang mit dem Klimawandel voraussichtlich häufiger auftreten werden. Um die Stabilität von Dämmen vorhersagen und verstehen zu können, müssen sowohl Sicker- als auch Überströmungsprozesse gemeinsam numerisch analysiert werden, da ihre kombinierte Wirkung sich von der Bewertung der einzelnen Prozesse unterscheiden kann.

Die Lattice-Boltzmann-Methode bietet einen neuen Ansatz für die Modellierung der Wechselwirkungen zwischen Strömungen in offenen Gerinnen und porösen Strukturen und ermöglicht präzise Simulationen von Phasenübergängen. Badarch et al. (2020) haben diese Methode erfolgreich zur numerischen Modellierung von Überströmung und Durchsickerung durch und über Dämme eingesetzt.

Ziel der vorliegenden Arbeit ist die Entwicklung eines Versuchsaufbaus zur Messung von Strömungsgeschwindigkeiten über permeablen Dämmen. Dazu werden Dämme mit unterschiedlichen Durchlässigkeiten verwendet und die Geschwindigkeit mittels Particle Image Velocimetry gemessen. Die Analyse der Geschwindigkeitsfelder zeigt, dass das durchlässigere Material (PPI45) an der stromaufwärts gelegenen Böschung und an der Böschungskrone höhere Geschwindigkeiten aufwies als das weniger durchlässige PPI60. Umgekehrt wies PPI60 am flussabwärts gelegenen Gefälle höhere Geschwindigkeiten auf, was aufgrund der größeren Wassertiefe zu erwarten ist. Die erfassten Geschwindigkeitsfelder sollen in naher Zukunft mit dem von Badarch et al. (2020) entwickelten numerischen Modell verglichen werden.

# TABLE OF CONTENTS

# LIST OF FIGURES

## LIST OF TABLES

# 1 Introduction

## 1.1 Motivation

Embankments play an important role in flood defence, in power generation and infrastructure. Their failure poses significant risks to populations residing in flood-prone areas. Depending on the material used, embankments can be categorized as erosive, non-erosive, or a combination of both, each with distinct failure characteristics. Non-erosive structures, such as those made of concrete, tend to fail abruptly without prior visible deformation. In contrast, earthen embankments, which are erosive, may breach due to surface erosion caused by overtopping from surges and waves, internal erosion, or sediment transport due to seepage, and morphological changes. (ASCE/EWRI Task Committee, 2011)

Earthen embankments breach due to overtopping (34%), foundation defects (30%) and piping (28%). With the increase in extreme and variable precipitation patterns due to global warming, the frequency of dam failures from overtopping is expected to rise (ASCE/EWRI Task Committee, 2011). In addition to the overflow the failure of embankments is influenced by the propagation of seepage through it. The permeability of the material significantly influences the propagation velocity of seepage, also referred to as flow through porous media (Rosenberry & Pitlick, 2009). Flow through porous media occurs in various contexts, including interactions between riverbeds and soils (Furman, 2008; Liang et al., 2020; Oka et al., 2008; Rosenberry & Pitlick, 2009), and flow through coastal defence structures (ASCE/EWRI Task Committee, 2011; Islam et al., 2019; Philip L-F Liu et al., 1999; Takahashi et al., 2019a) as well as in waterflooding processes in oil recovery (Liu et al., 2021; Sadeghi et al., 2018).

Embankments function as flood defence structures occurring in rivers, on land, or along coastlines. Predicting their failure necessitates the modelling of extreme scenarios and adjusting the design of protective measures accordingly. Various methods, including small-scale physical models, larger-scale field surveys, and computer-based models, are employed to estimate the failure of flood protection under extreme situations. However, physical models and field studies often have limitations due to the scale and complexity of the scenarios modelled. (Philip L-F Liu et al., 1999; Takahashi et al., 2019a)

Numerical models offer a valuable tool for simulating the complex interactions between fluids and soils (Philip L-F Liu et al., 1999; Takahashi et al., 2019a). As highlighted by Furman (2008) and Rosenberry et al. (2021) many numerical models across different applications simulate flow in distinct subsystems in order to simplify the model. Research on embankment stability often also considers seepage and overflow separately. However, combining these flows results in significantly higher embankment deformation. To achieve a more realistic deformation estimate, it is necessary to integrate both flows in the simulation (Takahashi et al., 2019b). This combined approach is already employed in oil recovery (Liu et al., 2021 and Sadeghi et al., 2018). Here the injection of water through wells into oil reservoirs, displaces oil near production well. This process is influenced by the permeability and porosity of the soil.

Computational fluid dynamics (CFD) methods are used to model the interactions between flow and soil, enhancing our understanding of these processes. Porous materials are very complex to model due to the heterogeneous distribution of their properties. CFD models simplify the resulting microscale processes by modelling them on a macroscale. Due to the exclusion of the microscale effects CFD methods struggle to accurately model phase transitions between soil and fluid. To address this, new numerical tools like the Lattice-Boltzmann Method (LBM) have been developed, offering robust modelling of fluid–fluid and fluid–soil interactions. (Furman, 2008; Sadeghi et al., 2018)

The ongoing research by Badarch et al. (in prep.) presents a numerical model utilizing the Lattice-Boltzmann Method (LBM) to simulate flow over and through porous media. This approach effectively handles flow through porous materials by incorporating liquid fractions as parameters. The model was validated in a previous work by Badarch et al. (2020) using a rectangular dam. A good agreement between calculated and specified permeability values could be demonstrated. Badarch et al. (2020) confirmed the model's performance and applicability with further tests across different flow scenarios, making it suitable for both microscale and macroscale simulations. Consequently, it provides a more accurate representation of the processes occurring during a flooding event at a defence structure, such as an embankment. This detailed understanding can subsequently be utilized to model breaching processes and to evaluate and improve the design of defence structures, specifically in the context of embankments. (Badarch et al. in prep., 2020)

In order to validate the numerical model in the ongoing work of Badarch et al. (in prep.) experimental measurements must be carried out and their results compared with those of the numerical modelling. On the one hand, the velocities of the overflow can be measured for this purpose. On the other hand, it is possible to measure the development of the bottom pressure inside the embankment and use this to determine the velocity of the seepage flow. In addition, the development of the water level can be measured in conjunction with the rising flow until a steady state is reached. From this, the velocities of the overflow can be determined.

In the ongoing research by Badarch et al. (in prep.) laboratory experiments were conducted at the Technical University of Vienna. An embankment made of PUR foam was tested in a flume, with water inflow, bottom pressure, and flow behavior being recorded (see Figure 1).

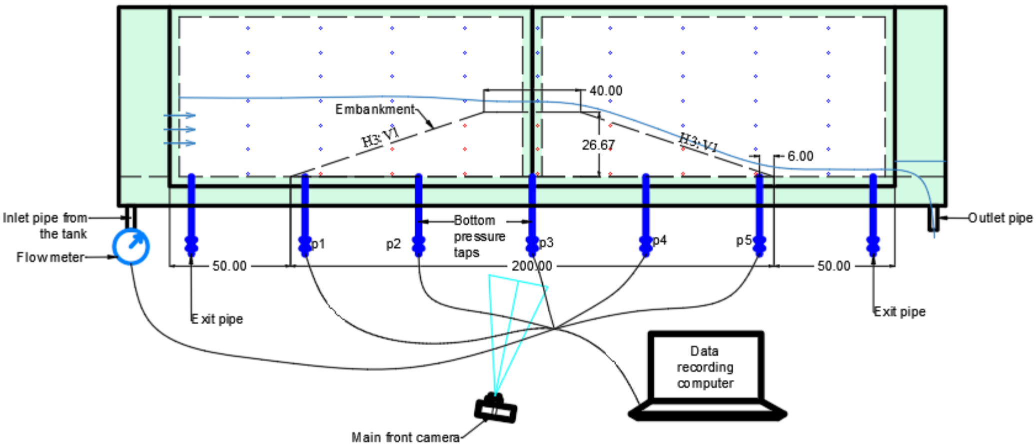


*Figure 1: Experimental setup including measurement devices and embankment used by* Badarch et al. (in prep.)

During the experiments, surface tension and capillary effects significantly influenced pressure and flow behavior. To mitigate this, soap was used to reduce surface tension, which helped improve flow infiltration. The main results compare the experimental and computational values of the bottom pressure development with an increasing discharge over time. However, discrepancies between experimental and modeled results still arose, attributed to differences in material properties, permeability, and boundary conditions. The study suggests incorporating these factors more effectively in future models to improve alignment between simulations and experiments. A complete summary of the preliminary work of Ayur can be found in the Appendix A.

## 1.2 Objectives

The first objective of this work is to measure the surface velocity over a permeable embankment and produce a data set which can be used to validate the numerical model developed by Badarch et al. (in prep.). Due to turbulence involved, accurately modelling surface flow is challenging and making a reliable experimental dataset crucial for improving the modelling approach. The experimental setup used in this work is the same as in Badarch et al. (in prep.) with a few adaptations made to ensure the success of the experiments and a good dataset.

The velocity distribution of the surface flow will be determined using Particle Image Velocimetry (PIV). To achieve this, microscopic particles are introduced into the water, illuminated by a laser, and their motion is recorded with a camera for analysis during post-processing. This measurement will produce a dataset containing the velocities field of the overflow along the embankment. Moreover, producing velocity profiles of the surface flow will allow for a more detailed assessment of the influence of seepage on the overflow behavior.

In addition, the permeability of the embankment material will be experimentally determined following the method used by Dietrich et al. (2009). This approach ensures that the exact same permeability is applied in both the numerical model and the experiment. Two different permeabilities will be tested for the embankment material.

The second objective of this work is to compare and analyse the differing resulting velocities of the surface flow when different permeabilities are used. The expected results will show the development velocities of the surface flow over the embankment. It is expected that the embankment with lower permeability produces higher water levels and therefore higher surface velocities. Conversely, the surface velocities over the embankment with higher permeability should be lower. Hypotheses for the different behavior of the surface flow can be developed using fundamental physical principles. However, no further experiments are conducted to investigate these differences in detail.

## 1.3 Structure

The structure of the following work is described below. Firstly, the experimental setup is introduced. For that, the adaptions which are made to optimize the experimental results from Badarch et al. (in prep.) are explained. In addition the setup had to be changed, so the velocity measurements with PIV can be conducted.

Afterwards the material used for the embankment and the used utensils for executing the PIV measurements are shortly presented and described. In a preliminary study the permeability of the material used for the embankment was determined. This is important to ensure the comparability with the numerical model used by Badarch et al. (in prep.) The preliminary study is shown in Appendix B.

In the following the method used to measure the surface velocity is introduced. The experimental technique Particle Image Velocimetry (PIV) is used to obtain the velocity distribution of the surface flow. The principle of how PIV works and the analysis of the is shortly explained. In the next part the experimental procedure presented.

The final chapter presents the results, beginning with the permeability values obtained from the preliminary experiments. This is followed by an analysis of the velocity distribution measured during the main experiments. A comparison of the permeability of two different materials is conducted to assess the impact of permeability on overflow velocity distribution.

The thesis concludes with an interpretation of the results, an error analysis, and a discussion of future work. Further experiments are recommended to clarify the influence of permeability on the interaction between seepage and overflow.

# 2 Experiments

This chapter describes the advancements made in the experiments originally conducted by Badarch et al. (in prep.). It outlines the new experimental setup, explains the measurement techniques, and describes the experimental procedures employed.

## 2.1 Experimental setup

The experiments of Badarch et al. (in prep.) were carried out in a cuvette (see Figure 2) that was already available in the hydraulic engineering laboratory at the Technical University of Vienna. The material for the embankment consists of PUR foam with 45 pores per inch (PPI), a permeability of 1.17x10-8 $m^2$, crest width of 40 cm, height of 26.7 cm and slopes of H3:V1. It has dimensions of 1000x2000x10 cm and consists of a riveted steel frame with glass panes embedded on one side. The cuvette is fed from the laboratory's water reservoir via a pump. The water is first supplied to a water reservoir approximately 3 meters above ground and then channelled into the experiment via a DN 5 pipe. The reservoir contains a flow diffuser designed to reduce turbulence. This means that a constant flow can be assumed in the experiments. There are seven outlets at the bottom of the cuvette, with pressure gauges connected to five of them to measure the bottom pressure curve. The flow is recorded with the main front camera and the data is collected and saved by a computer.

As the PIV technique for velocity measurement is introduced in this work, various adjustments must be made to the experiment so that the measurement can be carried out as accurately as possible and a good data set can be produced. The changes made are described below. The experimental setup was deliberately kept simple to ensure that the experiments could be carried out with minimal prior experience and without excessive complexity.

**Recirculation**

In Badarch et al. (in prep.) experiments, the water was pumped from the tank into the channel and returned to it (see Figure 2). It was not necessary to reuse the water for the measurements carried out, so the water system was sufficient for this purpose.

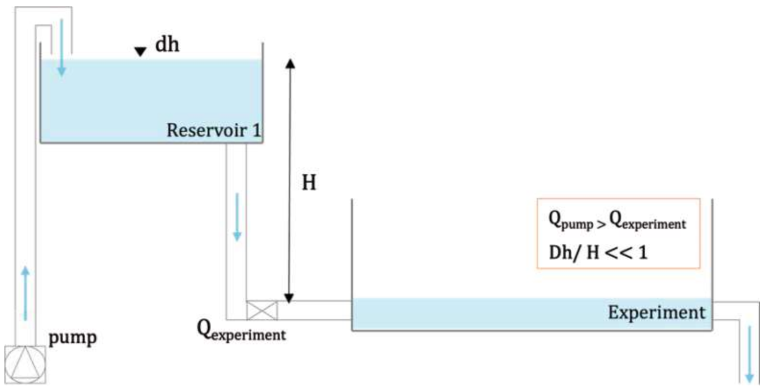


*Figure 2: Scheme of Badarch et al. (in prep.) experimental setup*

As part of the adaptation of the experiment, an additional water reservoir was posit Figure 3ioned below the reservoir 1 as in. This collects the water from the outlet of the cuvette and pumps the water back into the reservoir 1 using a Gardena pump. In order to maintain a constant water level in reservoir 1, an overflow was arranged via which the excess water runs into reservoir 2. This results in recirculation. The resulting advantages are that the system runs independently of the large pumps and additional material or sediment that is introduced into the water during the test does not end up in the reservoir. After completion of the tests, external disposal is possible depending on the load.

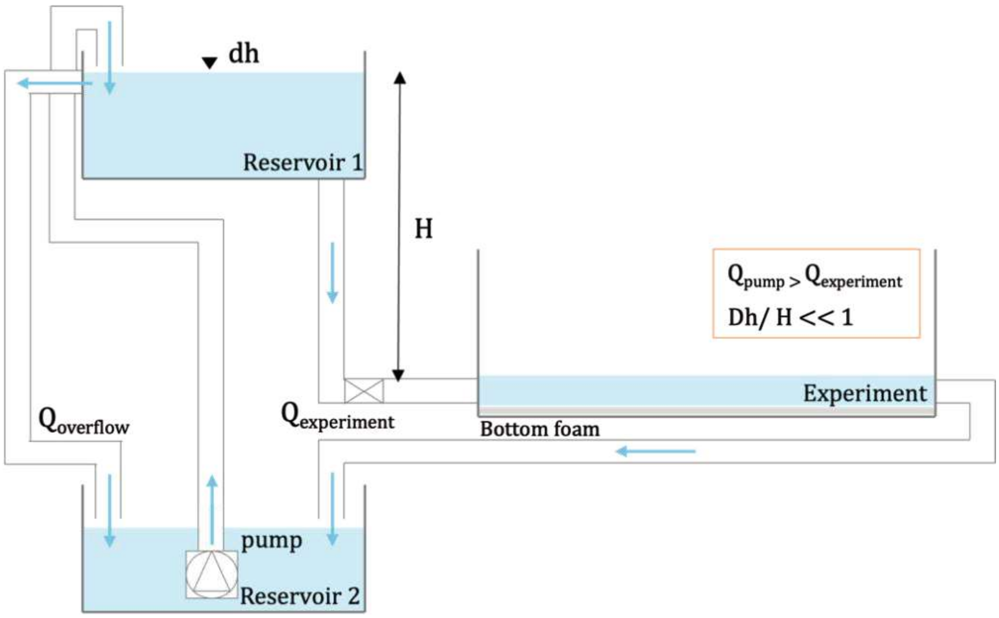


*Figure 3: Scheme of the adapted experimental setup for the improved experiments*

**Floor seal**

In the experiments of Badarch et al. (in prep.) at all bottom pressure measuring points, the pressure rises earlier than in the numerical modelling because there is a sheet flow between the bottom layer and the embankment. Within the modelling, it is assumed that the bottom layer is impermeable. In the experiment, however, the transition between the embankment and the subsoil is not completely impermeable, which leads to the premature increase in bottom pressure.

In this work in order to prevent a preferential sheet flow at the bottom boundary a type of floor seal is installed (see Figure 3). The seal consists of a foam material with a high permeability and was divided into several compartments using brass plates attached between them. The size of the compartments was chosen in such a way that the floor pressure gauges are each enclosed in the moth of a compartment. Made up of 6 identical pieces of foam, each attached and connected to brass plates. The dimensions of the individual compartments are 1 x 10.5 x 20 cm. The filter foam and the brass plates are tightly bonded with silicone.

**Velocity measurement**

In Badarch et al. (in prep.) experiments, the surface elevation and the bottom pressure were measured and used for the comparison with the numerical results. As the experimental and simulated results did not completely agree, a new experimental approach is being attempted. For this purpose, the surface velocity of the flow over the embankment is to be measured.

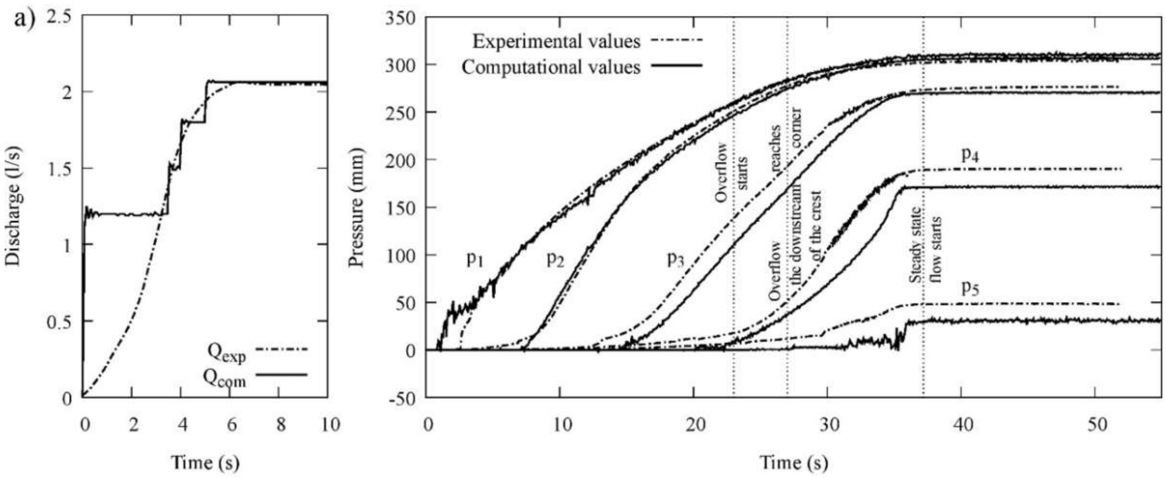


*Figure 4: Measurement of inlet discharge development (left); experimental and computational seepage (right)*

To analyse the properties of the overflow over the embankment, information about the velocity distribution is required. There are different methods to measure the velocity of flows. Due to the experimental set up and the geometry of the embankment in the context of this work, Particle Image Velocimetry (PIV) was chosen to determine the current flow field of the overflow. In order to make velocity measurement with Particle Image Velocimetry (PIV) possible, two necessities had to be met with the experimental setup: a recirculating system and completely dark conditions. The device to darken the setup is a box made of slats with dimensions of 2.2x3x3m. The box is closed all around with lightproof curtains to make the light from the laser visible to the camera.

**Camera positioning**

In the experiments from Badarch et al. (in prep.) the camera had a fixed position on a tripod. By using a tripod it is difficult to reproduce the exact same position. This can be a source of error in the measurement and lead to inaccurate results.

In the present work a precise positioning of the camera is required for the velocity measurement. Due to the size of the experiment, the velocity measurement cannot be carried out with a single shot. Instead, the various sections must be defined and the camera must be moved accordingly. Guide rails from the company Ibus, including guide carriages, were installed so that the camera can be moved seamlessly in all three axes. The carriage can be locked with a screw. The exact position of the camera and therefore the section being analysed can thus be reproduced.

*Figure 5: Photo of the adapted experimental setup to perform PIV measurements*

The resulting new experimental setup with all the adaptions made is shown in Figure 5. On the left side in the figure reservoir 1 and 2 and the pump that connects the two can be seen. In the centre you can find the cuvette in which the embankment is inserted and the velocity measurement is carried out. The rails on which the camera can move in all three directions is located in front of the flume. Around the flume you can observe the box with the curtains, which can be closed during the experiment.

## 2.2 Material

In the following the material used for the experiments is described. Firstly, the foam material used for the backfill and its properties are characterised. In addition, tracer particles, a camera and a laser blade are required as equipment for measuring the surface velocity.

### 2.2.1 Foam

Experiments to analyse flood defence structures can be carried out with different materials. The appropriate material is selected depending on what is to be investigated. If, for example, the failure of defence structures like embankments is to be investigated, a material is used with which the shear process can be modelled. In this thesis, however, only the seepage and surface flow are to be analysed. For this reason, a material was chosen that is available in different permeabilities and does not deform during the experiment. Filter foam is a good option in this case. The shape of the embankment is adapted to the standard structure of embankments and shaped to the appropriate proportions (see Figure 6).

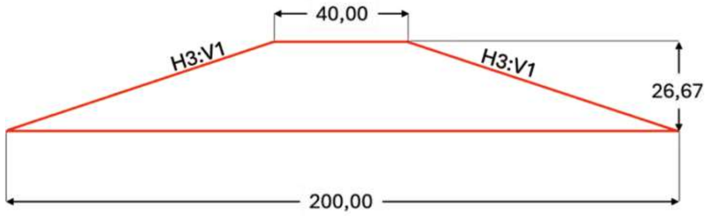


*Figure 6: Measurements of the embankment used in the experiments*

The material was ordered from the company PanaFoam and is available in different versions. The key figure used for this is PPI, which stands for pores per inch. Filter foam with PPI 45 and 60 was ordered. The permeability of the embankment cannot be determined directly using the PPI figure. This must therefore be determined in a preliminary test. The permeability must be known so that the same value can be used in the numerical model.

- Material: Polyurethan (PUR)
- Size: 45 and 60 PPI
- Company: PanaFoam

The permeability for the two different foams is shown in Table 1. The test setup for the preliminary tests to determine the permeability, the methods used and other relevant results are shown in Appendix B. There are explicit measuring devices and laboratory tests that have been developed to determine the permeability of porous material (f.e. magnetic resonance imaging). A new experimental approach was used in this case, which is very simple in its design and implementation and does not require any additional measuring equipment. (Dietrich et al., 2009)

*Table 1: Permeability for PPI 45 and PPI60*

| | PPI45 | PPI60 |
|---|---|---|
| PPI | 45 | 60 |
| K1 | -1,53E-09 | 1,31E-14 |

### 2.2.2 Tracer particles

In a preliminary study, the visibility of different sized particles was compared to each other. The particle size for the following experiments was then selected at 50 µm. The quantity of particles in the volume of water should be high enough to ensure that around 5-10 particles are visible in each interrogation window (Raffel et al., 2018). In the first experiments, the amount of particles was calculated as a function of the volume of water and the density of the particles.

Due to the long period of time in which the experiments were carried out, the amount of particles was not stable due to water evaporation and the adhesion of the particles. As the experiments progressed, small quantities of the particles were repeatedly added and the quantity of particles was checked visually using the camera images. It is important that the particles are clearly visible in the image, in order to reflect sufficient light. However, if there are too many, the individual particles can no longer be recognised in the analysis and the movements cannot be traced.

- Material: PSP, Polyamic Seeding Particles
- Size: 50 µm
- Company: Dantec Dynamics

### 2.2.3 Camera

The camera must fulfil various requirements. The frame rate should be sufficiently high so that the particle movement is visible even at higher speeds. Different cameras were tested and compared with each other in terms of frame rate, processing and handling (see Table 2). In terms of frame rate, all cameras were able to fulfil the requirements. The Ximea camera was chosen due to its size, its simple operation with the XiCamTool and its good video processing.

*Table 2: Comparison of the different cameras which were tested*

| Camera | Size | Operation | Video processing |
|---|---|---|---|
| Phantom (Highspeed camera) | Large and not very practical due to its size | Difficult to set up and move camera at tripod, operation tool available | High resolution, good contrast, extensive video data |
| Leica | Normal camera size | Easy to attach to the tripod | High resolution, good contrast, exposure time too short to recognise faster movements |
| Ximea | Small and easy to adjust position | Easy to attach to tripod; attachment to guide rails possible due to size, weight and geometry, operation tool available | High resolution, good contrast, sufficient exposure time |

Ximea Camera:

- Company: xiC Gen1+ Ricoh lens
- Framerate: 56 fps (max. 300)
- Resolution: 1250 x 2500
- Tool: xiCamTool
- Format: TIFF

### 2.2.4 Laser

Before carrying out the main experiments, the size of the area that the laser sheet can illuminate was tested. It was found that the experiment had to be divided into smaller areas, as the illuminated areas were limited by the laser and the camera. To avoid having to analyse too many areas, it was decided to combine two laser sheets. A homogeneously illuminated area of approx. 35 x 35 cm can be spanned with the two laser sheets. The lasers are attached to a holder that can be moved vertically and horizontally. The laser sheets are placed in a plane and fixed in such a way that they illuminate the area in the centre of the channel. Since the radiation intensity of the laser sheets is relatively low, the safety precautions for the experiments are not very stringent.

- Type: Compact Laser with Laser Sheet
- Colour: Green
- Intensity: 50 mW
- Company: MediaLas

## 2.3 Method

The following section outlines the technique determining the velocity field of the overflow over the embankment. The foundational principles of the measurement method will be explained, followed by a description of the experimental procedure.

### 2.3.1 Principle PIV

The velocity of gases and fluids is often determined by measuring parameters, as gases and fluids do not normally contain traceable particles that make the velocity of the flow visible. The velocity can be determined in various ways e.g. by measuring pressure, rotational speed or heat transfer. Although these measurement methods are easy to implement, they can change the flow velocity during the measurement and only provide localised results. Optical measurement methods however do not alter the flow and allow a velocity field to be measured over a larger area, being positioned outside the flow. By adding so-called tracer particles to the flow, the velocity is visualised. One of these optical measurement methods is PIV.

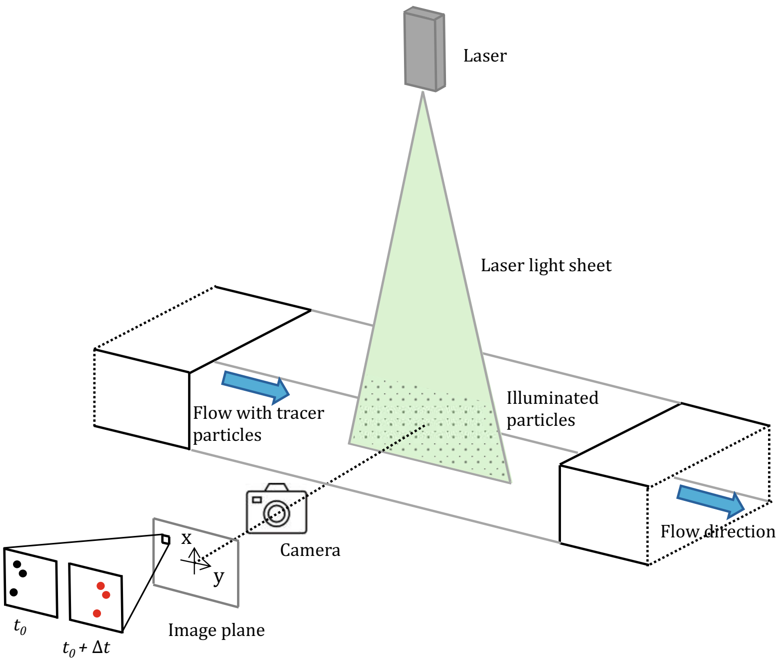


*Figure 7: Exemplary test setup for a PIV measurement with all necessary equipment* (based on Raffel et al., 2018)

Microparticles are added to a flow that is illuminated by a thin laser strip (2D). Several images are taken at very short intervals using a camera pointed at 90 degrees. In the analysis, the individual images are compared with each other in order to recognise the movement of the particles. The particle displacement is determined, and the velocity of the flow can be derived. A possible test setup for a PIV measurement with all relevant equipment such as laser sheet, imaging optics and tracer particles is shown in the following. (Raffel et al., 2018)

### 2.3.2 Technical equipment PIV

A PIV setup consists of tracer particles, a camera and a laser sheet. In the following section the most important information for the components which are used in the experiments is collected.

#### 2.3.2.1 Tracer Particles

Seeding, sometimes called tracer particles should be non-toxic, non-abrasive, non-volatile and chemically inert. Many different particles are available for PIV. The material choice depends on whether gases or fluids are being analysed. Furthermore, the type and intensity of the laser sheet influences the selection of the particles depending on the diameter and reflectivity. (Melling, 1997)

The accuracy of the determination of the velocity field depends on how precisely the particles follow the flow. The smaller the particle, the better it can follow the flow. However, the particles also require a certain size in order to reflect sufficient light. A size should be selected for the particles so that they follow the flow without delay and are clearly visible due to the amount of light they reflect. Furthermore, the particle size should not vary so that the light is being reflected evenly and with the same intensity from all particles. This increases the quality of the image. In frequent experiments a range from 1-500 µm has been used. (Melling, 1997)

Particles with very small diameters can only be used if the laser is strong enough and the camera is sufficiently sensitive. This is because the scattering ability of smaller particles is very low and otherwise no analysable images can be recorded. If sufficient sediment particles are present and they follow the flow well, no additional particles need to be added. In most situations, particles must be added to create sufficient contrast in the image and to ensure the particle size. (Raffel et al., 2018)

PIV measurements in liquids are often used in recirculating systems. The particles are dissolved in a suspension and can be added to the liquid in this form before the start of the experiments. This procedure allows the particles to disperse homogeneously inside the liquid (Melling, 1997). If the particles are to be separated from the liquid again after the experiments have been carried out, they can either be chosen slightly too light so that they settle on the edges and the surface or they can be chosen slightly too heavy so that they settle at the bottom of the reservoir and can thus be removed. (Raffel et al., 2018)

#### 2.3.2.2 Camera

A distinction can be made between two camera recording techniques. In the first method, the images of the particles are captured at different times on one image. The images therefore contain no information about the temporal sequence of the images, which is why methods must be used to interpret the movement of the particles. In the second method, an image of the illuminated particles is taken for each laser pulse. Here, the temporal sequence of the images is available, which makes the results much more reliable. (Raffel et al., 2018)

In recent years, CMOS -based cameras have become established for PIV applications. They have a high spatial resolution and enable images to be taken at intervals of a few nanoseconds. Very high readout rates are possible with CMOS sensors. (Melling, 1997)

#### 2.3.2.3 Laser

Lasers can produce monochromatic light with high energy density. To have a 2D vision of the propagating particles, the laser can be bundled into thin light sheets illuminating the tracer particles. A laser typically consists of three components: the laser material, the pump source and the mirror. The laser material can consist of gas, semiconductor or solid material. The pump source supplies energy to the laser material and thereby excites it. The mirror enables oscillation in the laser material. (Raffel et al., 2018)

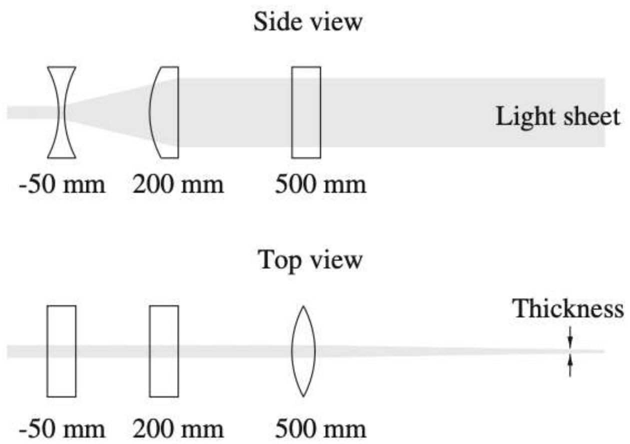


*Figure 8: Combination of different lens shapes to create a laser sheet* (Raffel et al., 2018)

Lenses can be arranged differently to create a laser sheet. The use of a cylindrical lens is particularly important to create the laser sheet. Depending on the type of laser, the laser sheet is created with 1-2 lenses and the third lens then determines the narrowness or thickness of the laser sheet (see Figure 8). (Raffel et al., 2018)

In compact lasers, the lens is integrated directly into the structure and can be used as a single product. Compact lasers are available in different versions. Point lasers illuminate a specific point, line lasers illuminate a 2D field and cross lasers illuminate a 3D field.

A laser sheet can also be created from two or more lasers combined with each other. To achieve this, lasers must match in intensity distribution, amplitude, width and shape. A complete intensity distribution of the lasers should be achieved in combination. Furthermore, the combination of two compact lasers as line lasers can enlarge the existing laser sheet so that a more comprehensive section can be illuminated and thus also examined. (Raffel et al., 2018)

### 2.3.3 Analysis PIV

The open-source python package "OPYFLOW" is used to analyse the velocities over the porous embankment. In the first step good features to track () which have f.e. a good optical contrast is used to detect the particles in every frame. In the second step the optical flow is used to calculate the movement of the particles that were recognised in preprocessing. Optical flow is the pattern between the apparent movement of objects on a camera between two frames. Using this alternative tracking procedure may improve both efficiency and accuracy on velocity estimations compare to classical PIV approaches (G. Rousseau & Ancey, 2022). A full description of this optical flow velocimetry method is provided in Appendix B.

### 2.3.4 Experimental procedure PIV

The experimental setup was divided into different recording sections. As the two laser sheets together can cover a well-lit area of 35x35 cm, the embankment was divided into 6 sections of 33 cm each (see Figure 9). The first two sections are completely covered by the camera (33x33cm). In the following sections V3-V6, the camera is positioned at a shorter distance from the experiment. The speeds increase here, and the region of interest must have a higher resolution so that the particle movement is visible in the video processing. Furthermore, the light intensity of the particles from a greater distance is too low. The measurement is carried out when constant pressures and velocities have been established, i.e. the steady state has been reached.

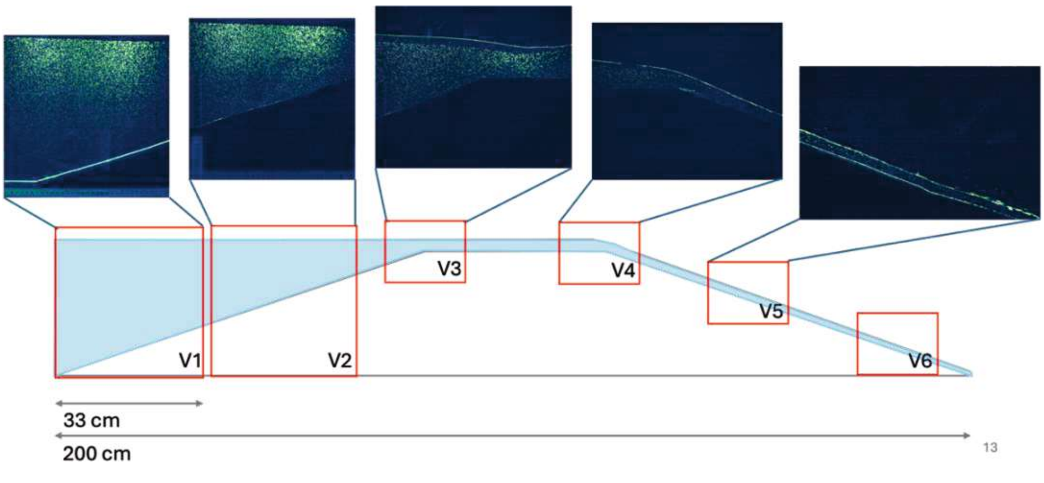


*Figure 9: Camera positions along the embankment where the videos were recorded for PIV analysis*

To begin the experiment, the pump in Reservoir 2 is activated, and water is allowed to flow until it overflows from the elevated Reservoir 1. After this initial setup, the channel should be opened within approximately 10 seconds, adjusting the flow rate to 2 l/s. As the system stabilizes, the embankment becomes saturated, leading to overflow and establishing a stationary flow condition, indicated by the absence of further changes in the pressure and velocity distribution. Next, the laser devices are positioned so that they face each other, ensuring that they are centered within the channel. Once the lasers are properly aligned, the camera is placed onto the guide carriage in the first pre-determined position. The camera is then connected to the computer, and the operational software is launched.

Subsequently, a chessboard is placed within the plane of the laser, ensuring it is correctly aligned with the beam. The camera's focus is then adjusted accordingly to achieve a balanced and clear image. At this point, it is important to document all key experimental parameters, including the precise flow rate, the defined Region of Interest (ROI), and the exact position of the camera on the guide carriage. To minimize external interference, curtains are drawn around the experimental setup.

Within the XiCamTool software, the settings for the Region of Interest (ROI), frames per second (FPS), exposure time, and grain size are configured. Additionally, the storage location and file type for the recorded data are specified, and the video settings are saved. Once the system is ready, a video recording is made for a duration of 15 to 20 seconds. After the video is captured, the camera is repositioned to a new location on the guide carriage, and the process is repeated to collect further data.

# 3 Results

The analysis of the recorded data was carried out using the Python package OpyFlow. The analysis parameters, which are presented in Appendix ,were determined through an iterative process. An example of this iterative process for the first position is described in Appendix B.

By iteratively adjusting the parameters during the analysis and post-processing the image data prior to analysis, high-quality and meaningful data can be produced. The following section presents this process, and the observations made during image processing and analysis. In the first step using the image processing software Fiji, the contrast and brightness of the video data can be improved before analysis. The image data is adjusted to enhance particle detection and movement tracking by the algorithm. For each analyzed section, 200 frames are imported as an image sequence into the program. Brightness is increased, and contrast is enhanced. Additionally, a mask can be created, allowing the subsequent analysis to focus solely on the region where water movement occurs, effectively filtering outliers in the air or within the embankment.

In the next step, the region of interest (ROI) is defined in OpyFlow. It is important to ensure that the ROI is not smaller than the mask defined in Fiji. The ROI and the mask must have the same number of pixels in both the x and y directions. If the analyzed image sections are further subdivided, new masks must be created that correspond in size to the new areas. The size of the search window for optical flow parameters can be individually adjusted. By default, a window of 12x12 pixels is analyzed. The smaller the search window, the smaller the particles the algorithm can detect and track their movement. This parameter can be utilized to analyze velocities even in cases of low video quality.

Additionally, the velocity range in the x and y directions can be configured. Before applying this filter, the analysis is initially conducted without it, and all the calculated values in both the x and y directions are plotted over time. This allows for the identification of outliers (very high or very low values). The velocity range is then adjusted to focus solely on the predominant velocities. As the video progresses, the range is gradually increased to account for rising velocities.

However, it is necessary to restrict the detection area with a mask, limiting it to where the movements of interest occur. Otherwise, excessive motion, such as dust particles moving through the air, may be detected. The quality level should be reduced simultaneously to avoid detecting non-existent movements. During the analysis, the values for each analyzed image pair are interpolated across the entire region on a grid. Once all image pairs have been analyzed, the values can be interpolated a second time across the region. This step helps to evenly distribute the values across the examined area and eliminate point outliers. During the second interpolation, the analysis parameters can be further refined. If the interpolation radius is increased compared to the initial analysis, the resulting interpolation is much smoother, with fewer outliers.

### 3.1 Results and Comparison PPI 45 and PPI60

In all experiments, a constant flow rate of 2.0 l/s was maintained to analyze the material-dependent evolution of flow velocity across the cross-section and enable a comparison between the two materials with differing permeabilities. In all positions, the difference between the two materials was highlighted by subtracting the velocity values of PPI 60 from the corresponding values of PPI 45. This method allowed for a clear identification of differences in velocity distribution. The calculated value is absolute, so the difference is always positive. The resulting difference fields enabled a focused analysis of the materials' impact on flow distribution along the embankment and provided a visual representation of deviations in flow velocity. Additionally, velocity profiles were recorded at a quarter and half of the flow path length at all measurement positions, allowing for a more detailed investigation of the flow field. The velocity profiles clearly show which material achieves higher velocities at the same position. Velocity fields were generated at six selected positions along the embankment model. Details regarding the examined area sizes, camera settings, and scaling are summarized in Table 3.

*Table 3: Details about the different camera positions*

| Position | Region of Interest (cm) | Camera Position (x\|y\|z) | FPS | m/px |
|---|---|---|---|---|
| P1 | 33 x 30.5 | 6.7 \| 59 \| 34 | 56.65 | 0.00039 |
| P2 | 32.5 x 22.5 | 36.6 \| 56.8 \| 34 | 56.65 | 0.00039 |
| P3 | 31 x 13 | 71.2 \| 62.5 \| 23.3 | 56.65 | 0.00025 |
| P4 | 23 x 10.2 | 112.5 \| 62.5 \| 15.2 | 95.03 | 0.000187 |
| P5 | 23.5 x 11 | 141.5 \| 52.2 \| 23.3 | 102.32 | 0.00028 |
| P6 | 24.9 x 12.5 | 175.5 \| 43.75 \| 23.3 | 102.32 | 0.000275 |

At positions P1 to P3, the flow divides into surface runoff, which flows over the embankment structure, and seepage flow, which penetrates and percolates through the embankment material. At positions P3 and P4, part of the flow becomes visible on the embankment crest, where surface runoff predominates. At positions P4 to P6, both the surface runoff, which flows along the downstream slope, and the seepage flow, which exits the embankment material, are observable. At these points, both flows converge again and exit the test channel together.

#### 3.1.1 Results Position 1

In Figure 10 and Figure 11, the first investigated position on the embankment is depicted. The slope has a gradient of 1:3 on both sides. In the left graphic for PPI 60, the velocity field of the overflow over the embankment using PPI 60 at Position 1 is displayed. The graphic to the right shows the overflow over the embankment with PPI 45. The water level in the left graphic (PPI 60) is 0.31m, which is about 1 to 1.5 cm higher than in the right graphic. Over the observed distance, the water level decreases by approximately 1 mm downstream in both experiments.

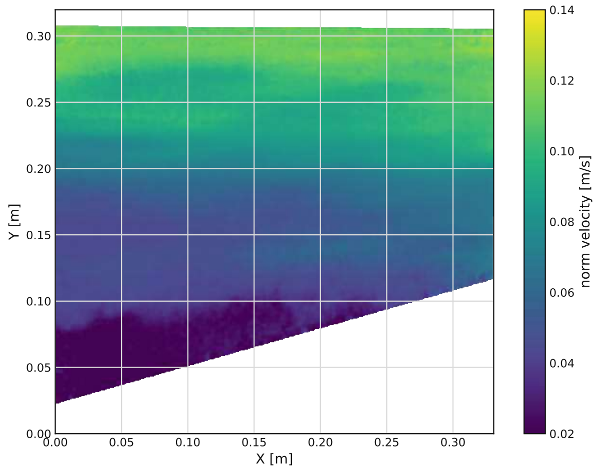


*Figure 10: Velocity field at Position 1 for PPI60*

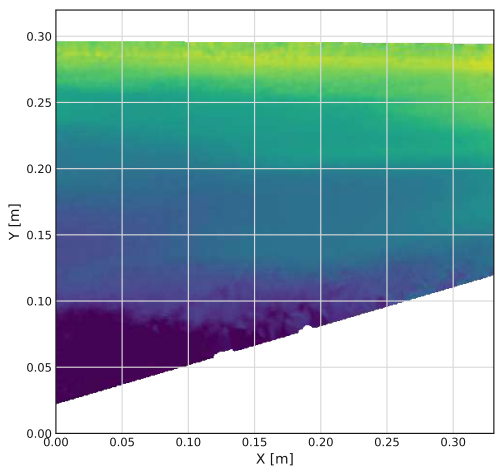


*Figure 11: Velocity field at Position 1 for PPI45*

In both cases, flow velocity increases as water depth decreases. With PPI 60, velocities range from 0.02 m/s in the deepest area to a maximum of 0.12 m/s just below the water surface. Slightly higher velocities are observed with PPI 45, varying between 0.02 m/s and 0.14 m/s. To enable a more direct comparison between the two materials, the difference in velocity fields was calculated. The slightly higher velocities of PPI 45 were subtracted from the velocities at all points in the PPI 60 field, resulting in a difference field that visualizes the discrepancies between the two materials and flow conditions (Figure 12). Additionally, velocity profiles at quarter and half of the position were plotted for both materials in one graphic to compare the velocity distribution over the height (Figure 13).

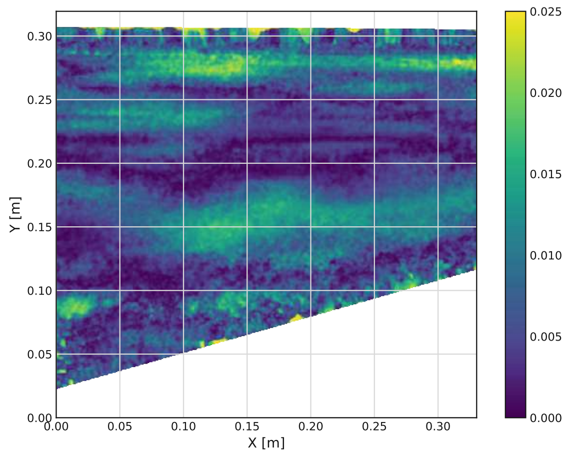


*Figure 12: Velocity change between PPI45 – PPI60 at Position 1*

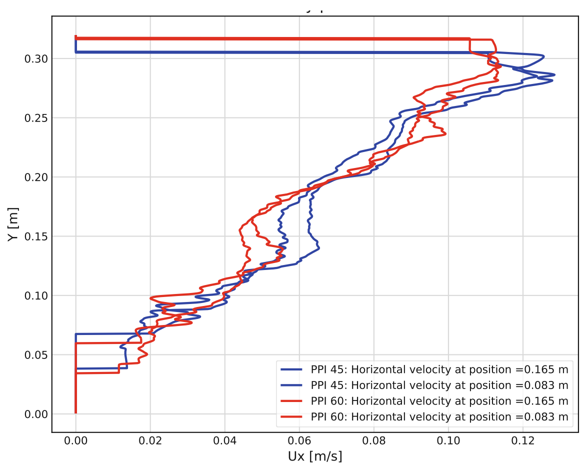


*Figure 13: Velocity profiles at x=0.165m and x=0.083m at Position1 for PPI45 (blue) and PPI60 (red)*

As seen in Figure 12, the velocity difference between the two materials varies from 0.0 to 0.025 m/s, with increasing values near the water surface. This increase can be attributed to the fact that velocities for PPI 45 rise more sharply with decreasing water depth. This trend is observed at all investigated points of the position, except in the central region. At position x = 0.17 m and y = 0.15 m, the difference is particularly pronounced at 0.018 m/s. At the same x-position but at y = 0.2 m, i.e., closer to the water surface, the velocity difference decreases significantly. Here, the velocities at both positions are nearly identical. Appendix C shows the change in velocity between PPI 45 and PPI 60 in the x- and y- directions for all positions.

The velocity profiles show that flow velocity strongly depends on water depth (Figure 13). Directly beneath the water surface, the velocity reaches its maximum and decreases with increasing depth. Upon impact with the embankment, the velocity drops to 0 m/s. For both materials, a quadratic relationship between flow velocity and water depth is observed.

The velocity profiles for PPI 45 are depicted in blue, and those for PPI 60 in red. Between Y = 0.2 m and Y = 0.14 m, both materials show a significant decline followed by a rise in velocity, with values fluctuating around 0.01 m/s. The further downstream the position, the higher the velocities in the profile. The velocity profiles of PPI 45 are consistently above those of PPI 60 across the entire water depth. A notable difference is seen directly below the water surface, where PPI 45 velocities exceed those of PPI 60 by 0.14 m/s to 0.2 m/s. Overall, the velocity profiles cover a range of 0.11 m/s.

### 3.1.2 Results Position 2

The velocity fields at Position 2 represent the middle section of the upstream side of the embankment slope. The water level of the overflow over the PPI 60 (Figure 14) material is 0.21m, approximately 1.5 cm higher than for PPI 45 (Figure 15). Additionally, the water level shows a slight drop of about 1 cm. In both images, velocities ranging from 0.025 to 0.2 m/s are measured.

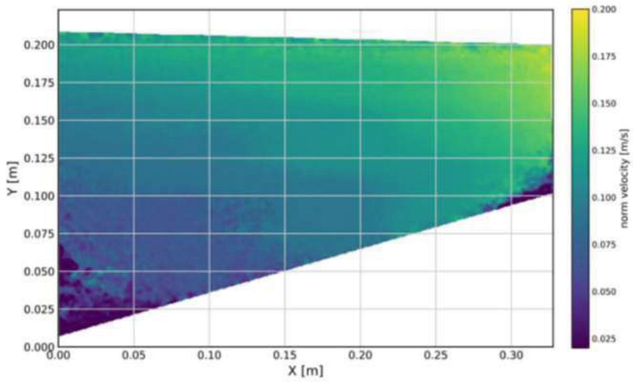


*Figure 14: Velocity field at Position 2 for PPI60*

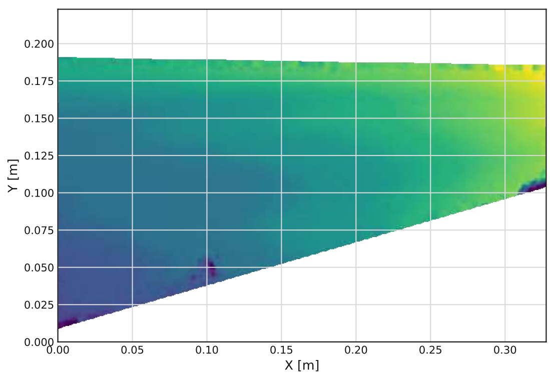


*Figure 15: Velocity field at Position 2 for PPI45*

As seen in Figure 16, the velocity difference ranges between 0 and 0.05 m/s and increases downstream. Notable differences are particularly evident in the lower outer corners. Below the water surface, the difference is about 0.035 m/s, decreases halfway down the water column, and rises slightly above the embankment.

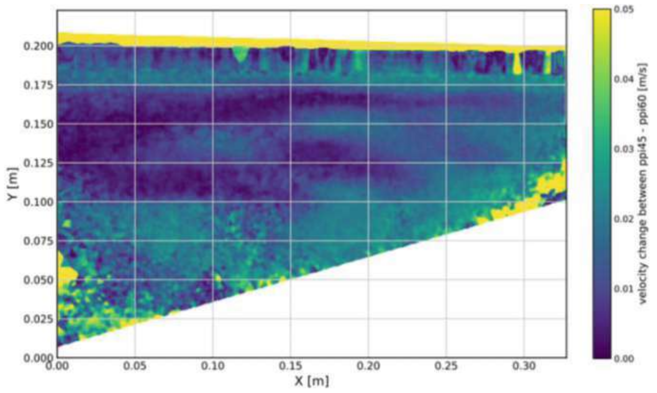


*Figure 16: Velocity change between PPI45– PPI60 at Position 2*

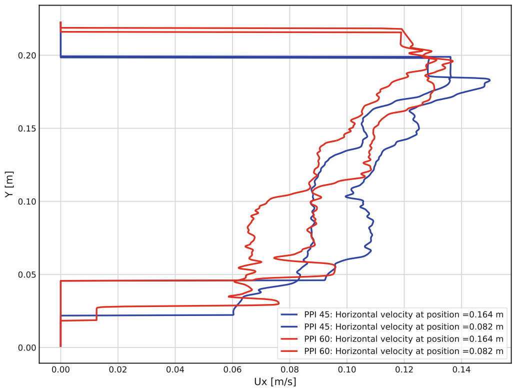


*Figure 17: Velocity profiles at x=0.164m and x=0.082m at Position 2 for PPI45 (blue) and PPI60 (red)*

A direct comparison of the velocity profiles (Figure 17) shows that the velocities for PPI 60 (displayed in red) are generally lower, ranging between 0.06 and 0.15 m/s. For PPI 45 (shown in blue), the values range from 0.06 to 0.165 m/s. As observed at Position 1, the profiles in the middle of the water depth (at Y = 0.13 m) show a drop and subsequent rise in velocity. Particularly for PPI 45, this drop in the middle of the profile at y = 0.12 m is clearly visible with a reduction of about 0.01 m/s. The profiles for both materials are steeper compared to Position 1, with the velocity range spanning 0.07 m/s.

Positions 1 and 2 are spatially adjacent, allowing a comparison of velocities at the transition areas. In Position 1, velocities at the right edge ranged between 0.05 and 0.11 m/s, while similar values were measured at the same location in Position 2. For PPI 45, velocities at the transition to Position 2 range from 0.05 to 0.13 m/s. In Position 2, velocities at the left edge vary between 0.06 and 0.13 m/s.

### 3.1.3 Results Position 3

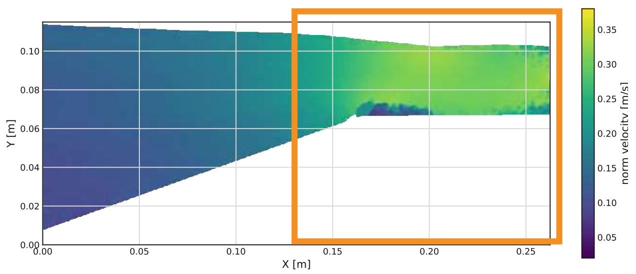


*Figure 18: Velocity field at Position 3 for PPI60; Area marked in orange is examined in more detail*

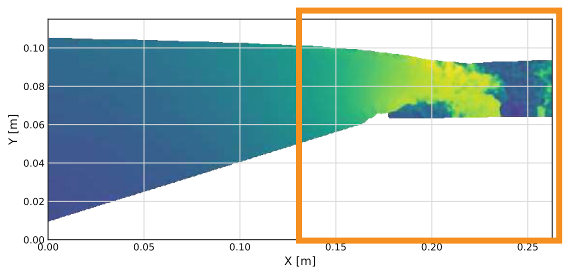


*Figure 19: Velocity field at Position 3 for PPI45; Area marked in orange is examined in more detail*

At Position 3, the final section of the upstream slope of the embankment, the transition to the embankment crest, and the first 0.08m of the crest are depicted. For PPI 60, velocity values between 0.10 and 0.33 m/s are measured, which is also visible in the velocity profile in Figure 18. In Figure 19 for PPI 45, velocities range between 0.10 and 0.37 m/s. In both illustrations, the measured values show a clear increase in the flow direction. Compared to the previous positions, a larger increase in velocities across the cross-section is observed here.

Additionally, sudden changes in velocity occur for both materials after the transition to the embankment crest. For example, between x = 0.17 m and x = 0.21 m, the velocity drops to 0.12 m/s. Another velocity drop at x = 0.23 m can be seen for PPI 45. To investigate the flow conditions in this position more precisely, the analyzed area was narrowed. The selected section now extends from x = 0.13 m to the outer right edge (marked in orange).

The velocity change between the two materials can be seen in Figure 20. It ranges between 0.01m/s and 0.03m/s. In the left corner where velocity drops in the velocity fields can be seen the velocity change is out of the considered range. In the velocity profile (see Figure 21), it is evident that the difference between the profiles in the examined area is significantly greater compared to the previous positions. The profiles are no longer in a similar velocity range but spread across a broader velocity distribution. The difference between the individual profiles is about 0.01 to 0.015 m/s. For PPI 45, the profiles are approximately 0.02 m/s above the measured values of PPI 60. The decrease in velocity across the increasing cross-section is clearly noticeable.

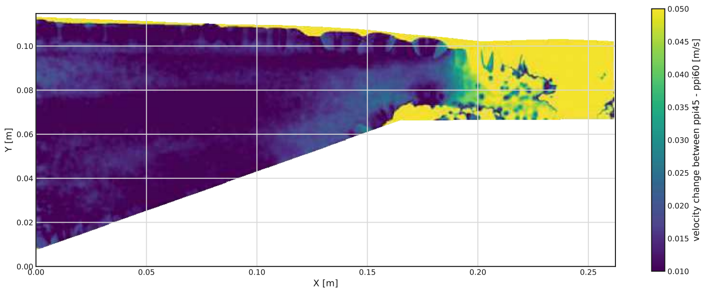


*Figure 20: Velocity change between PPI45 – PPI60 at Position 3*

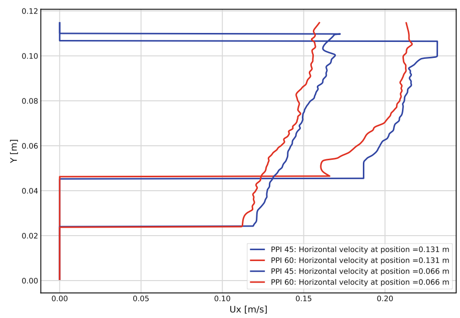


*Figure 21: Velocity profiles at x=0.038m and x=0.083m at Position 3 for PPI45 (blue) and PPI60 (red)*

In the area after the start of the embankment crest, which was examined in more detail in this section, the previously observed velocity drop is no longer evident (Figure 22 and Figure 23). Furthermore, no sudden decreases in flow velocity are observed for PPI 45 at the right edge downstream compared to the entire section. The velocity range can be adjusted for this area and consequently fewer outliers, which lead to a sudden velocity drop, are taken into account. A consistent velocity field can be identified, with the velocity across the entire area rising to maximum values between 0.3 and 0.38 m/s.

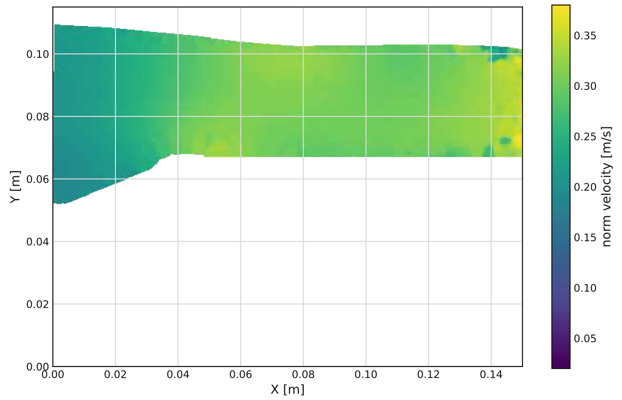


*Figure 22: Velocity field for orange marked area at Position 3 for PPI60*

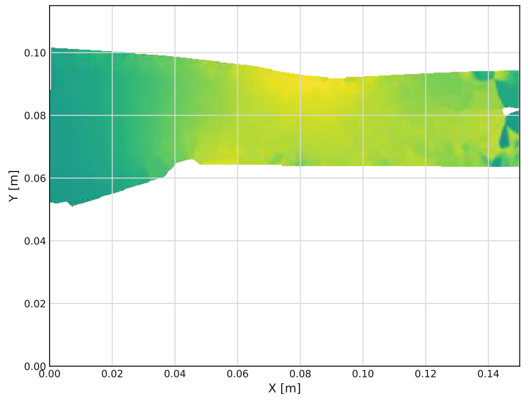


*Figure 23: Velocity field for orange marked area at Position 3 for PPI45*

From the beginning of the embankment crest, the velocity remains constant while the water level slightly decreases. The curvilinear drop in the water level occurs at x = 0.09m for PPI 60 and at x = 0.08m for PPI 45, with the drop in water depth being more pronounced for PPI 45 than for PPI 60. The highest velocities for both materials are measured below the falling water level, with a maximum of 0.32 m/s for PPI 60 and 0.38 m/s for PPI 45. In all examined areas, the velocities of PPI 45 exceed those of PPI 60. Up to the start of the embankment crest, the velocity difference between the materials is about 0.01 to 0.015 m/s. After the embankment crest, however, the velocities for PPI 45 rise significantly and are about 0.06 m/s higher than those of PPI 60 at the peak values.

### 3.1.4 Results Position 4

In Position 4, the transition from the crest of the embankment to the downstream slope is examined. The right section of the embankment crest, the transition to the slope, and the first 0.12m of the downstream slope are visible. At PPI 60, the flow velocity on the embankment crest is 0.45 m/s (Figure 24). In comparison to the velocities at the beginning of the embankment crest in Position 3, which were 0.325 m/s, a significant increase in velocity is observed along the embankment crest. Immediately behind the crest, velocities of up to 0.7 m/s develop. At the right edge of the area, at x = 0.175m, values of up to 0.95 m/s are measured.

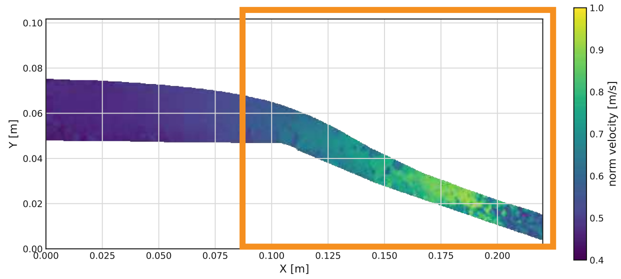


Figure 24: Velocity field at Position 4 for PPI60; Area marked in orange is examined in more detail

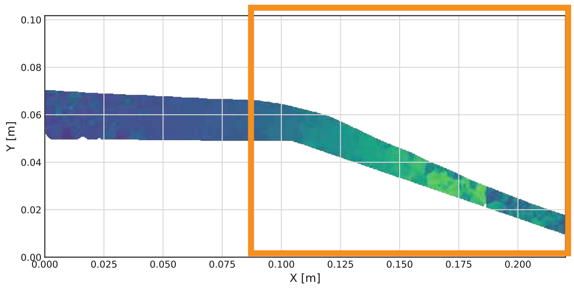


Figure 25: Velocity field at Position 4 for PPI45; Area marked in orange is examined in more detail

At PPI 45 (see Figure 25), a significant increase in velocity behind the crest can also be observed. The flow velocity on the crest is 0.55 m/s and increases immediately after the end of the embankment crest to 0.8 m/s. Like Position 3, information on velocity is missing in the right edge area for both materials. To enable a more detailed analysis of the area behind the crest, the investigated section is further narrowed down and focused on the downstream slope (marked in orange).

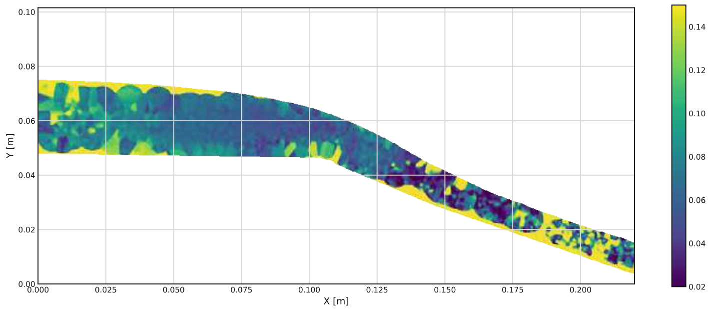


Figure 26: Velocity change between PPI4 – PPI60 at Position 4

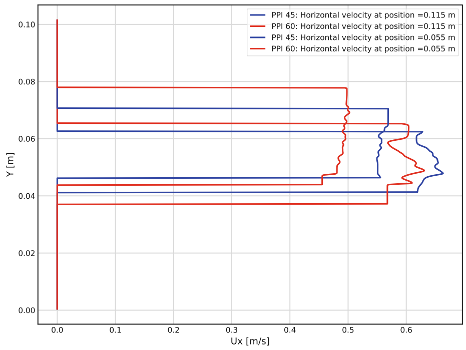


Figure 27: Velocity profiles at x=0.055m and x=0.115m at Position 4 for PPI45 (blue) and PPI60 (red)

The velocity change in Figure 26 ranges between 0.02 and 0.12m/s. The change between the two velocity fields decreases over the distance in Position 4. Differences of 0.1 m/s between the velocity profiles of the same material are observed at positions x = 0.055 m and x = 0.115m (Figure 27). In addition to the observation that the velocity change decreases, the difference in the velocity profiles decreases too. At the crest and at the beginning of the of the downstream crest the velocities for PPI45 are higher. The difference between the materials decreases and in the right bottom PPI60 reaches higher velocities. It is particularly striking that the velocities at PPI 60 increase more rapidly and reach values of up to 0.95 m/s in the right edge area, which are 0.15 m/s higher than those of PPI 45. Both materials show a steep increase in the velocity profiles. Compared to Positions 1 to 3, the velocity drop across the pressure height is less pronounced in this position.

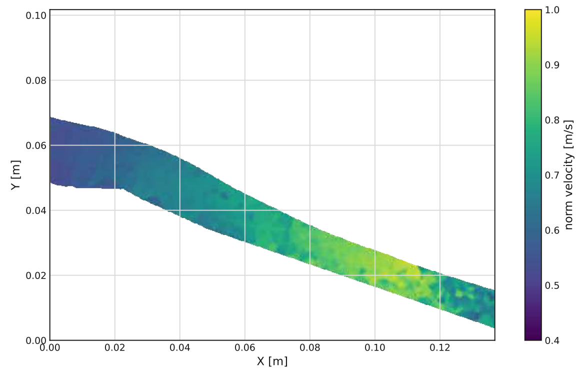


*Figure 28: Velocity field for orange marked area at Position 4 for PPI60*

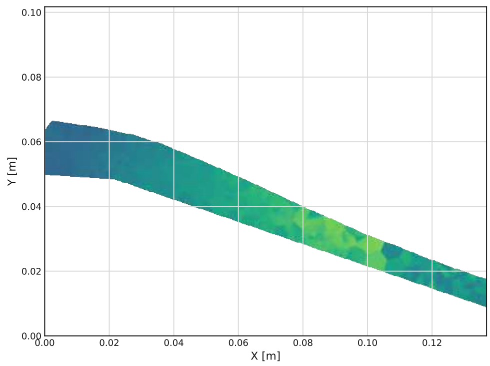


*Figure 29: Velocity field for orange marked area at Position 4 for PPI45*

The analysis parameters were adjusted to capture the velocity field in the right edge area of Position 4 (Figure 28 and Figure 29) more precisely. Velocities of up to 0.95 m/s were measured at PPI 60, and up to 0.87 m/s at PPI 45. The velocities at PPI 60 surpass those of PPI 45 by 0.07 m/s. Despite the adjustments to the examined area and the parameters the velocity values drop unexpectedly in the right edge area. It is noted that the water level is slightly higher at PPI 60 than at PPI 45.

### 3.1.5 Results Position 5

Position 5 and 6 are located in the middle and at the end of the downstream slope. In Position 5, both materials show a further increase in velocity. At PPI 60, the velocity increases from 1.1 m/s to 1.5 m/s (Figure 30), while the velocities at PPI 45 range between 1.0 m/s and 1.3 m/s (Figure 31). This indicates a lower increase and generally lower values compared to PPI 60. The velocities at PPI 60 are significantly higher than those at PPI 45 in this position. The water level for both materials is about 1 cm, with the water level at PPI 60 being about 1 mm higher than that of PPI 45. At PPI 45, the water level no longer shows a clearly defined line and instead exhibits several turbulences (see Figure 34).

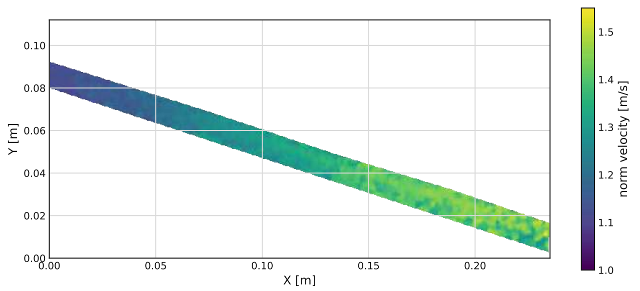


*Figure 30: Velocity field at Position 5 for PPI60*

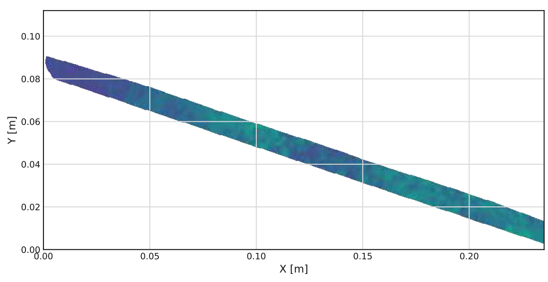


*Figure 31: Velocity field at Position 5 for PPI45*

The velocity change between the materials increases while the water propagates further downstream (see Figure 32). The velocity profiles in Figure 33 also show that the values for PPI 60 are higher than those for PPI 45. At a quarter of the position the velocities profiles show that values for PPI 60 are 0.1m/s higher. In the middle of the cross-section, the velocities for PPI 60 are 0.2 m/s higher than those for PPI 45. Both profiles illustrate a very steep increase, with velocity decreasing only slightly with increasing water depth. The velocity remains nearly constant across the profile.

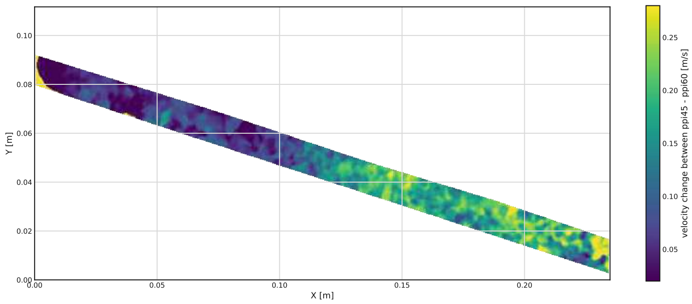


Figure 32: Velocity change between PPI45 – PPI60 at Position 5

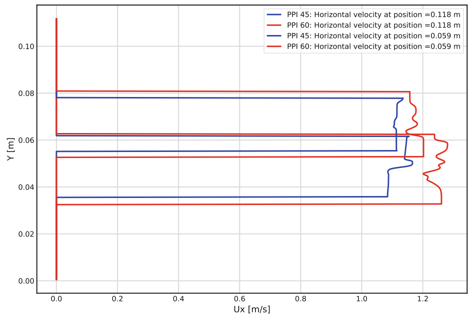


*Figure 33: Velocity profiles at x=0.059m and x=0.118m at Position 5 for PPI45 (blue) and PPI60 (red)*

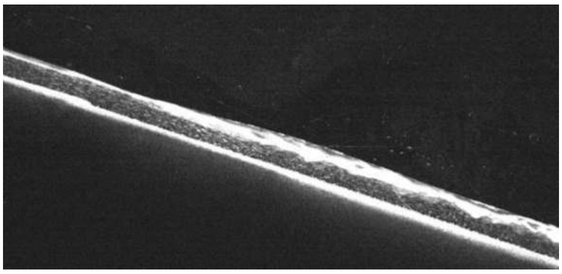

*Figure 34: Video frame at Position 5 for PPI45 showing the water level*

### 3.1.6 Results Position 6

In Figure 35, a velocity increase from 1.35 to 1.55 m/s is shown for PPI 60. For the material PPI 45, the velocities increase from 1.11 to 1.35 m/s (Figure 36). In both cases, an increase in velocity of 0.1 m/s compared to the previous position is observed. The water level for both materials is 1 cm. It is noticeable that the water level in Figure 39 appears turbulent and churned, a behavior already observed for the material PPI 45 in the previous position.

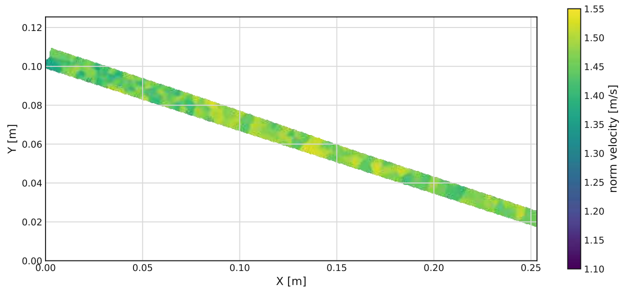


*Figure 35: Velocity field at Position 6 for PPI60*

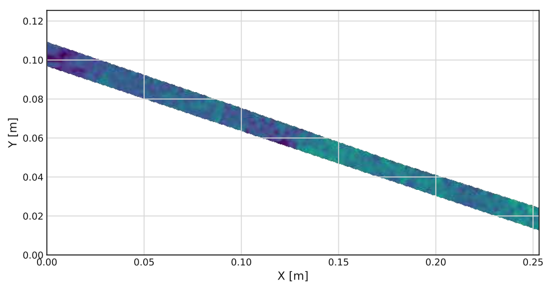


*Figure 36: Velocity field at Position 6 for PPI45*

The velocity change between the two materials decreases in flow direction (see Figure 37). In the bottom right corner, the lowest velocity change of 0.15m/s can be measured. The velocity profiles (Figure 38) from the quarter at x = 0.063m and at the center of the cross-section at x = 0.127m again clearly illustrate the difference between PPI 60 and PPI 45. The velocities for PPI 60 are significantly higher than those for PPI 45, with a difference of 0.3 m/s. For both materials, a steep increase or decrease in velocity with increasing water depth is observed. It can be assumed that the same velocity value applies to each profile across the entire water depth.

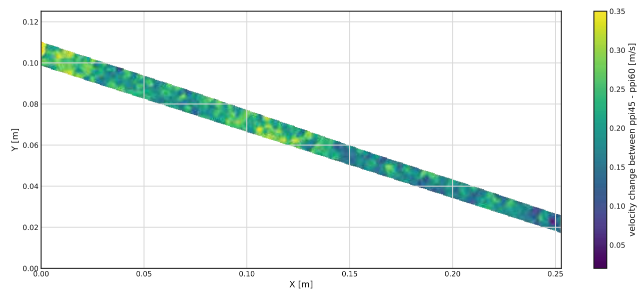


*Figure 37: Velocity change between PPI45– PPI60 at Position 5*

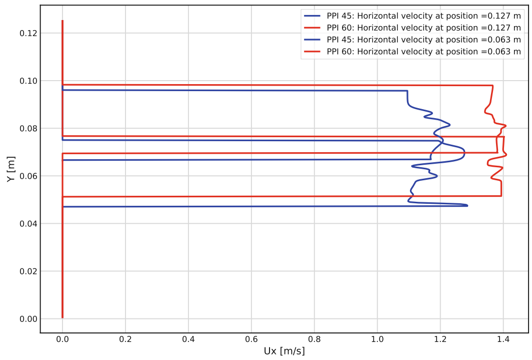


*Figure 38: Velocity profiles at x=0.063m and x=0.128m at Position 6 for PPI 45 (blue) and PPI60 (red)*

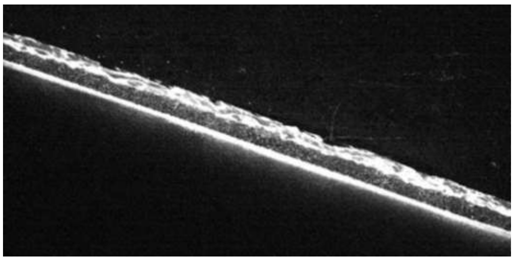

*Figure 39: Video frame at Position 6 for PPI45 showing the water level*

### 3.1.7 Summary of Results

The analysis of velocity distributions along the embankment in the various positions shows clear differences between the materials PPI 45 and PPI 60.

In Positions 1 to 3, which cover the upstream slope, the lowest velocities were recorded, with a minimum of 0.02 m/s. In these areas, the velocity for PPI 45 was consistently at least 0.01 m/s higher than for PPI 60. The velocity profiles showed a significant decrease in velocity with increasing pressure height.

At the end of Position 3, where the upstream slope ends and the embankment crest begins, a marked decrease in velocity is observed. The right edge area of this position proves to be particularly challenging, as the velocity increase was so strong that a precise analysis in this area was difficult. Therefore, this position was further subdivided, and a separate analysis of the right edge area could determine a clear velocity field.

In Position 4, which follows the embankment crest from Position 3, the downstream slope began. At the crest and at the beginning of the downstream slope the velocities fpr PPI 45 remain higher than PPI 60. For the first time, higher velocities were measured in the right corner of the area at PPI 60 compared to PPI 45. In this area, the right edge also had to be considered separately to correctly capture the strong increase in velocity.

Positions 4 to 6 recorded much steeper velocity profiles compared to the previous positions. In these positions, the velocities remained nearly constant over the water depth. Particularly in positions 5 and 6, the velocities were higher for PPI 60 than for PPI 45. The difference between the two materials increased along the embankment, with the maximum velocities of up to 1.55 m/s at PPI 60 reached in position 6.

In summary, the observations show that PPI 60 exhibits significantly higher velocities in the later positions along the embankment compared to PPI 45. The velocity profiles become steeper, and the differences between the two materials increase as one moves further along the embankment.

# 4 Discussion

## 4.1 Classification of results

The present study of the video data pursues two central objectives: Firstly, to compare the velocity fields of overflow for two materials with different permeability characteristics. One material is nearly impermeable, while the other has higher permeability. This approach allows for the analysis of the influence of seepage flow as a function of permeability. Secondly, the study aims to evaluate whether the chosen experimental setup, in conjunction with Particle Image Velocimetry (PIV), provides reliable and accurate results for capturing the velocity fields. This will be discussed in more detail in Chapter 5.

Regarding the embankment, three flow situations are observed. In positions 1 to 3, a portion of the main flow infiltrates the embankment as seepage flow, while the remainder flows over the embankment. The amount of infiltrating water is determined by the permeability of the embankment material, which in turn influences the volume of overflow water and the formation of water depth. At the right edge of position 3, the embankment crest begins, extending to position 4, where only overflow occurs. In positions 4 to 6, the overflow flows down the embankment slope while the seepage flow exits the embankment. An interaction between overflow and seepage flow is expected here, leading to increased turbulence. It is also assumed that the behavior of the overflow is influenced by the surface texture and roughness of the embankment material. The turbulence observed on the water surface in the video data supports this assumption.

In positions 1 to 3, a higher water level was measured for the material PPI 45 compared to PPI 60. The water level at PPI 60 consistently remains about 1 cm above that of PPI 45. This higher water level could suggest that flow velocities are higher at PPI 60. However, measurements indicate that velocities are actually higher at PPI 45.

This could be due to a greater proportion of the main flow infiltrating the embankment at PPI 45, which is attributed to the lower pore count in the material, resulting in higher permeability. This relationship was confirmed by preliminary experiments on permeability. The higher permeability of PPI 45 results in a less pronounced transition between overflow and seepage flow compared to the less permeable material PPI 60. It is hypothesized that seepage flow and overflow partially move together at PPI 45, leading to an overall higher water level. This may explain why higher velocities were measured for PPI 45 in positions 1 to 4. In contrast, overflow velocities at PPI 60 are lower, which correlates with a lower water level and results in lower flow velocities.

Another explanation for the higher velocities at PPI 45 is the differently pronounced vertical momentum transfer. Since a portion of the flow infiltrates the embankment at PPI 45, the momentum exchange is disrupted. The localized infiltration of the flow into the embankment could reduce the length of the so-called mixing length over which momentum is transferred. At the nearly impermeable material PPI 60, however, the momentum can spread up to the water surface, leading to more uniform velocities across the entire flow profile. A larger mixing length results in lower maximum velocities, while a smaller mixing length, as seen at PPI 45, leads to higher maximum velocities since the upper water layers are not reached and the velocity is not reduced there.

In positions 4 to 6, located on the embankment slope, the measured velocities for PPI 60 are higher than for PPI 45. Here, the water level at PPI 60 is again above that of PPI 45, leading to the expected higher velocities. Additionally, the water level at PPI 45 shows increased turbulence, likely due to the greater roughness of the material. The material of PPI 45 has larger pores, resulting in increased surface roughness due to the material's texture. In contrast, PPI 60 has a smoother and more uniform surface due to its smaller pores. In these positions, steep velocity profiles develop, indicating strong turbulence and mixing throughout the water depth. Above the embankment surface, there is a sudden and significant increase in velocity, which only slightly increases towards the water surface.

The study indicates that the permeability of the embankment material significantly impacts the flow conditions. The more permeable material (PPI 45) leads to higher velocities and stronger interactions between overflow and seepage flow, whereas the less permeable material (PPI 60) exhibits more uniform velocity profiles due to its lower permeability. Additionally, the surface roughness of the materials affects turbulence and flow velocities. Overall, the results confirm that both the permeability and roughness of the embankment material substantially shape the dynamics of water flow.

## 4.2 Error Analysis

The following describes potential factors that may have caused distortions in the results. First, the analysis using OpyFlow is discussed, followed by an examination of the experimental procedure and setup.

With each additional interpolation step and parameter adjustment, the accuracy of the results decreases. Nonetheless, the analyses can be performed with the chosen parameters due to the plausible sizes and distributions of the velocity values. It is essential, however, to always verify the plausibility of the results. Additionally, particle deposits on the glass wall of the experimental flume were observed, affecting the recording quality. To make the particle movements detectable for the algorithm, contrasts in the recordings had to be reduced. This also made dirt and scratches on the glass wall visible, preventing the algorithm from detecting movements in these areas. As a result, even after parameter adjustments, no velocity values could be assigned in certain areas.

The recorded videos had to be adjusted post hoc in terms of brightness and contrast to make particle movements more visible. The low intensity of the used laser facilitated handling and conducting the experiments but required additional post-processing of the video data. Furthermore, defects or contamination were only evident during the post-processing of the recordings, sometimes necessitating a repetition of the experiments.

The amount of particles was determined based on a general rule of thumb in the experimental planning and added to the water. However, since the water reservoirs are open, water evaporates over time, leading to changes in particle concentration between experiments. This caused fluctuations in particle quantity, as the experiments were not conducted simultaneously.

The analysis of the material PPI 45 posed a particular challenge due to the blue color of the material. The laser was reflected more strongly by the blue foam, resulting in uneven light distribution in the image. Increasing the brightness during image post-processing created the impression that the embankment surface appeared bulging in the center of the image. Additionally, the laser sheet's light cone was more visible in the edge areas, making particle movement detection more difficult.

Although curtains were used during the experiments to protect against external light sources, a narrow light strip was visible at the overlap points of the curtains due to reflections on the glass wall. These reflections only became apparent during image post-processing and prevented the determination of flow velocities in these areas, leading to an incomplete velocity field.

Finally, experimental conditions varied with each video recording, requiring re-adjustment of the analysis parameters for each position. This time-consuming process reduced the efficiency of the experiments and complicated data collection.

# 5 Conclusion

## 5.1 Summary

Using the experiments and the applied Particle Image Velocimetry (PIV) technique, velocity fields were generated for the entire area above the embankment. The resulting velocity fields for the two materials were compared and interpreted. Due to the differing permeabilities of the materials, it was possible to observe how permeability influences the velocity field of the overflow.

On the upstream slope and the dike crest (up to position 3), the velocities were higher for PPI 45 than for PPI 60. From position 4 onwards, located on the downstream slope, the velocities were higher for the less permeable material, PPI 60. Additionally, the water level was higher in all positions for PPI 60 compared to PPI 45. Turbulence and vortices were observed on the water surface at positions on the downstream slope.

The same experimental setup, flow conditions, and material permeability were transferred to the numerical model. The modelling results can be compared with the experimental findings to assess their consistency. If discrepancies are found, adjustments may need to be made to either the experiment or the model.

During the PIV measurements, it was established that their results were sufficient enough to validate the numerical model from Badarch et al. (in prep.) For this reason and due to time constraints, the other experimental measurments like bottom pressure measurements were not performed for this thesis.

### 5.2 Future development

To improve the suitability of the experimental setup and ensure more consistent experimental conditions, all experiments should be conducted within a limited time frame. This minimizes time-dependent variables such as evaporation and ensures that experimental conditions remain consistent. Additionally, using materials with different permeabilities but the same color could help reduce unwanted reflections and optical effects that might affect the flow analysis. A wider laser that illuminates the light field more broadly would improve particle visibility across the entire flow profile, particularly in the edge areas and deeper water layers. A finer subdivision of the analysis areas could also lead to more precise and meaningful results, as local variations in flow would be captured in greater detail.

Ideally, the experimental conditions should be designed to minimize external light entering the experimental flume. This would not only increase contrasts in the recordings but also minimize reflections on the glass wall of the flume. A diffusely scattering laser could help avoid light cones and make particle movement more visible both in the center and at the edges of the flow field. Darker materials for the embankment could also contribute to reducing light reflections and more clearly defining the embankment's contours, improving the accuracy of the analysis.

The suitability of the methodology can be further improved by finer subdivision of the examined flow areas. The range of measured velocities varies considerably, leading to reduced accuracy. A finer subdivision of the analysis areas could reduce this variability and filter out lower velocity values that appear as outliers. This would result in more homogeneous velocity fields without sudden drops in speed, enhancing the reliability of the results.

To better understand interactions between seepage flow and overflow, additional experiments should be planned where flow velocities are measured at the same water depth over both impermeable and permeable materials. These investigations could provide more insight into the extent of interaction between seepage flow and overflow and its effects on the flow profile.

## Sources

ASCE/EWRI Task Committee. (2011). Earthen Embankment Breaching. *Journal of Hydraulic Engineering*, *137*(12), 1549–1564. https://doi.org/10.1061/(ASCE)HY.1943-7900.0000498

Badarch, A., Blanckaert, K., & Fenton, J. D. (n.d.). *Lattice Boltzmann models for the combined flow over and through porous media*.

Badarch, A., Fenton, J. D., & Tokuzo, H. (2020). A Free-Surface Immersed-Boundary Lattice Boltzmann Method for Flows in Porous Media. In *GeoPlanet: Earth and Planetary Sciences* (pp. 23–31). Springer Science and Business Media Deutschland GmbH. https://doi.org/10.1007/978-3-030-37105-0_2

Bischelmaier, G. (2011). *Simulation des Strömungsverhaltens in einer Lamellendichtung mittels porösem Medium*.

Cocci, A. (2021). *Bachelorarbeit Durchströmung von verschiedenartig porösen Medien*. TU Wien .

Cours INSA. (n.d.). *Vélocimétrie par Imagerie de Particule Particle Image Velocimetry (PIV)*.

Dietrich, B., Schabel, W., Kind, M., & Martin, H. (2009). Pressure drop measurements of ceramic sponges-Determining the hydraulic diameter. *Chemical Engineering Science*, *64*(16), 3633–3640. https://doi.org/10.1016/j.ces.2009.05.005

Furman, A. (2008). Modeling Coupled Surface–Subsurface Flow Processes: A Review. *Vadose Zone Journal*, *7*(2), 741–756. https://doi.org/10.2136/vzj2007.0065

Islam, M. R., Hayano, K., & Rahman, M. A. (2019). Insights into Effects of Seepage on Failure of Breakwater Mound: Experimental and Numerical Investigations. *Indian Geotechnical Journal*, *49*(5), 531–542. https://doi.org/10.1007/s40098-019-00356-8

ISP GmbH. (2024a, September 8). *Technisches Datenblatt PPI45 Polyester*. https://isp-schaum.de/pdf/ISP_DB_ES_45PPI.pdf

ISP GmbH. (2024b, September 8). *Technisches Datenblatt PPI45 Polyether*. https://isp-schaum.de/pdf/ISP_DB_ES_45PPI_AE.pdf

ISP GmbH. (2024c, September 8). *Technisches Datenblatt PPI60 Polyether*. https://isp-schaum.de/pdf/ISP_DB_ES_60PPI.pdf

Körner, C., Thies, M., Hofmann, T., Thürey, N., & Rüde, U. (2005). Lattice Boltzmann model for free surface flow for modeling foaming. *Journal of Statistical Physics*, *121*(1–2), 179–196. https://doi.org/10.1007/s10955-005-8879-8

Liang, D., Zhao, X., & Soga, K. (2020). Simulation of overtopping and seepage induced dike failure using two-point MPM. *Soils and Foundations*, *60*(4), 978–988. https://doi.org/10.1016/j.sandf.2020.06.004

Liu, S., Zhang, C., & Ghahfarokhi, R. B. (2021). A Review of Lattice-Boltzmann Models Coupled with Geochemical Modeling Applied for Simulation of Advanced Waterflooding and Enhanced Oil Recovery Processes. *Energy and Fuels*, *35*(17), 13535–13549. https://doi.org/10.1021/acs.energyfuels.1c01347

Melling, A. (1997). Tracer particles and seeding for particle image velocimetry. In *Meas. Sci. Technol* (Vol. 8). http://iopscience.iop.org/0957-0233/8/12/005

Oka, F., Kimoto, S., Kato, R., Kodaka, T., Oka, F., Kimoto, S., Kato, R., Sunami, S., & Kodaka, T. (2008). *A Soil-Water Coupled Analysis of the Deformation of an Unsaturated River Embankment due to Seepage Flow and Overflow*. https://www.researchgate.net/publication/237212056

OpenCV. (2024a, August 27). *Feature Detection - Image Processing* . https://docs.opencv.org/4.x/dd/d1a/group__imgproc__feature.html#ga1d6bb77486c8f92d79c8793ad995d541

OpenCV. (2024b, August 27). *Optical Flow*. https://docs.opencv.org/3.4/d4/dee/tutorial_optical_flow.html

OpenCV. (2024c, August 27). *Shi-Tomasi Corner Detector & Good Features to Track*. https://docs.opencv.org/4.x/d4/d8c/tutorial_py_shi_tomasi.html

Philip L-F Liu, B., Lin, P., Chang, K.-A., & Sakakiyama, T. (1999). *NUMERICAL MODELING OF WAVE INTERACTION WITH POROUS STRUCTURES*.

Raffel, M., Willert, C. E., Scarano, F., Kähler, C. J., Wereley, S. T., & Kompenhans, J. (2018). *Particle Image Velocimetry A Practical Guide Third Edition*.

Rosenberry, D. O., Engesgaard, P., & Hatch, C. (2021). Hydraulic conductivity can no longer be considered a fixed property when quantifying flow between groundwater and surface water. In *Hydrological Processes* (Vol. 35, Issue 6). John Wiley and Sons Ltd. https://doi.org/10.1002/hyp.14226

Rosenberry, D. O., & Pitlick, J. (2009). Local-scale variability of seepage and hydraulic conductivity in a shallow gravel-bed river. *Hydrological Processes*, *23*(23), 3306–3318. https://doi.org/10.1002/hyp.7433

Rousseau, G., & Ancey, C. (2022). An experimental investigation of turbulent free-surface flows over a steep permeable bed. *Journal of Fluid Mechanics*, *941*. https://doi.org/10.1017/jfm.2022.310

Rousseau, G. P. D. M. (2019). *Turbulent Flows over Rough Permeable Beds in Mountain Rivers: Experimental Insights and Modeling*.

Sadeghi, R., Shadloo, M. S., Hopp-Hirschler, M., Hadjadj, A., & Nieken, U. (2018). Three-dimensional lattice Boltzmann simulations of high density ratio two-phase flows in porous media. *Computers and Mathematics with Applications*, *75*(7), 2445–2465. https://doi.org/10.1016/j.camwa.2017.12.028

Shi, J., & Tomasi, C. (1994). *Good Features to Track*.

Takahashi, H., Morikawa, Y., Mori, N., & Yasuda, T. (2019a). Collapse of concrete-covered levee under composite effect of overflow and seepage. *Soils and Foundations*, *59*(6), 1787–1799. https://doi.org/10.1016/j.sandf.2019.08.008

## APPENDIX A: Preliminary experiments by Badarch et al. (in prep.)

In the ongoing research of Klicken oder tippen Sie hier, um Text einzugeben.Badarch et al. (in prep.) the numerical model could be validated for a rectangular embankment. Applying it for a more natural case, small-scale experiments using a typical geometry were carried out in the laboratory at the Technical University of Vienna. The set-up, measurements, procedure and the results are presented in the following section to analyse the potential improvement of the experiments.

### Experimental Setup

The experiments were conducted in a cuvette at the hydraulic engineering lab of the Technical University of Vienna (see Figure 40). The embankment, made from PUR foam with 45 pores per inch (PPI) and a permeability of 1.17x10-8 m$^2$, measured 1000x2000x10 cm. It was housed in a steel frame with glass panes and had a crest width of 40 cm and a height of 26.7 cm. Water was supplied from a reservoir via a pump and flowed through a DN 5 pipe, with a flow diffuser reducing turbulence to ensure a constant flow. The cuvette had seven outlets at the bottom, with pressure gauges connected to five for bottom pressure measurements. The flow data was captured by a front camera and stored on a computer.

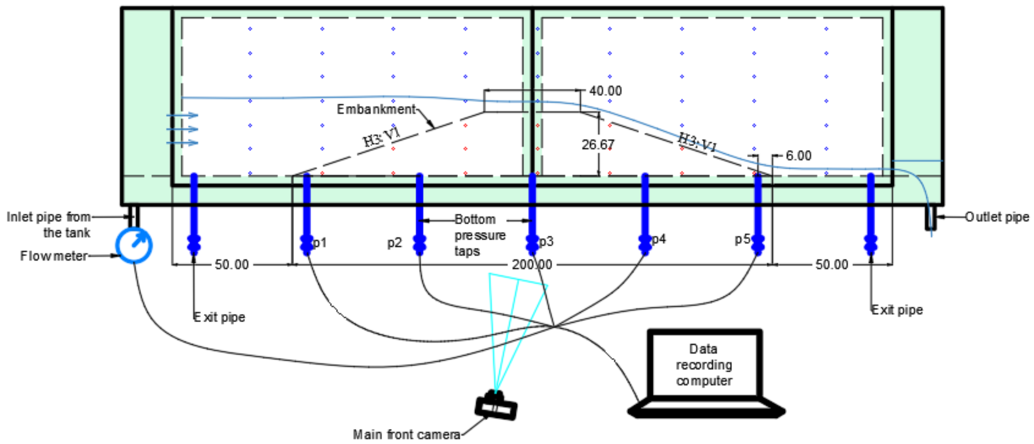


*Figure 40: Experimental setup including measurement devices and embankment used by* Badarch et al. (in prep.)

Furthermore, pressure measuring points are distributed across the entire cross-section of the embankment to determine the pressure of the seepage flow using a manometer. The surface elevation and the seepage are documented with a camera.

### Experimental procedure

The experiment is started the moment the inlet discharge is opened. From this point onwards, inlet discharge and bottom pressure are measured. The camera runs the whole time to record the phreatic and free surfaces as well as the pressure distribution in the embankment via the manometer.

The experiment is carried out three to five times to reduce uncertainties. At the beginning, when the flume has just been opened, the flow is still unsteady. The embankment is completely dry, and the flow must first infiltrate through the embankment and flow over it until the embankment is completely saturated and a constant pressure and velocity distribution are established. From the point at which the embankment is saturated with water and there is less to no air inside the material, the flow can be described as steady. Before each test, the soil pressure sensors and the manometer must be calibrated so that no measurement errors are caused by air trapped in them. The individual measured values are recorded as required, stored and analysed afterwards. The flow rate for the experiments was set at 2.0 litres per second.

The embankment body is made of foam. Material-specific properties are to be expected due to the porous medium. The material is well suited for multiple and exact implementation, as no geometric deformation occurs due to flow. However, the embankment body is buoyant due to the high proportion of air voids, which is why the embankment was designed to be 10.5 cm wider than the 10 cm channel, so that it is held in place by compression and cannot float up. Furthermore, the material has a capillary effect that should not be neglected, which cannot be prevented and is therefore assumed to be 14-15 mm. The surface tension and the swelling tension are further parameters that are specific to this material. The surface tension was reduced with the help of soap. This improved the infiltration of the embankment surface, but the surface tension within the embankment could not be completely reduced.

**Results**

The results from the preliminary experiments of Badarch et al. (in prep.), presented below, are compared with the model results. During the initial tests, significant surface tension was observed in the embankment. To address this issue, a preliminary test involving soap was conducted to reduce the surface tension.

**Preliminary Study: Use of soap to reduce surface tension**

The tests were started with a flow rate of Q = 3.7l/s. Figure 41 shows clearly that when soap is used the surface tension of the seepage flow within the embankment decreases noticeably. Therefore, there is also a change in the velocity field. The surface tension depends on the structure of the material inside and on the surface, the flow rate and the saturation. It can be observed that the lower the flow rate, the lower the surface tension. As a result, a flow rate of 2.05 l/s was set and used in the further progress of the experiments. During the preliminary study, it was also determined that the measurement from the pressure sensor has an uncertainty of +-5 mm and from the inlet discharge of +- 0.004 l/s which can be taken into account in the analysis afterwards.

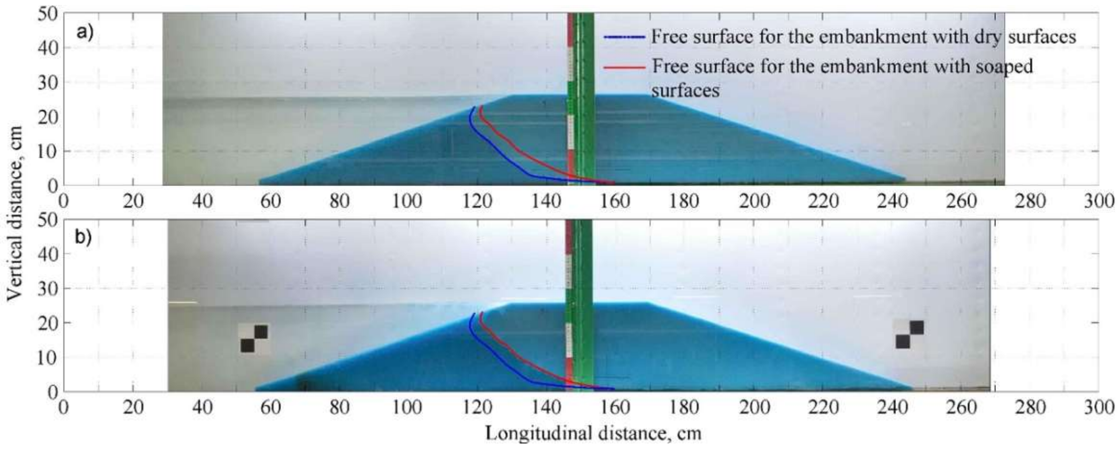


*Figure 41: Seepage flow inside embankment comparing dry surfaces with soaped surfaces*

**Measurement of inlet discharge and bottom pressure**

The inlet discharge and the development of the bottom pressure were measured simultaneously. In Figure 42 below, the measured and modelled values are shown in the same graph. Based on the result of the measurements, it can be observed that the pressure in the sensors increases in a staggered manner at different time periods. This is due to the seepage flow, which first must propagate through the embankment so that a constant pressure and a steady state can be achieved. As the water height above the pressure measuring points varies, different pressures occur.

The inlet discharge is increased to 2.0 l/s within 10 seconds. The recording of the experimental values shows that a uniform increase in the inlet discharge is not possible. The results of the model (solid line) and the experiment (dashed line) are almost identical for the first two measuring points of the bottom pressure. The pressure rises earlier in all measurement points than in the model, which is due to a sheet flow between the embankment and the subsurface. The slightly higher pressure at p1 in the experiment can be attributed to the higher inlet discharge in the experiment, as can be seen in the left-hand graph. The measured values for p1 and p2 are then approximately in the same range. The bottom pressure sensors p3, p4 and p5 measure higher pressures everywhere in the experiment. This may be due to surface tension, capillarity and air trapped in the pores as well as irregular pore structure and size occurring in the experiment.

The pressure in p3 rises after 15 seconds when the seepage flow has reached the centre of the embankment. When the water level reaches the top of the embankment and starts overflowing, the pressure rises very quickly due to surface tension and capillarity until a steady state is reached at 38 seconds: a constant pressure prevails in all pressure sensors.

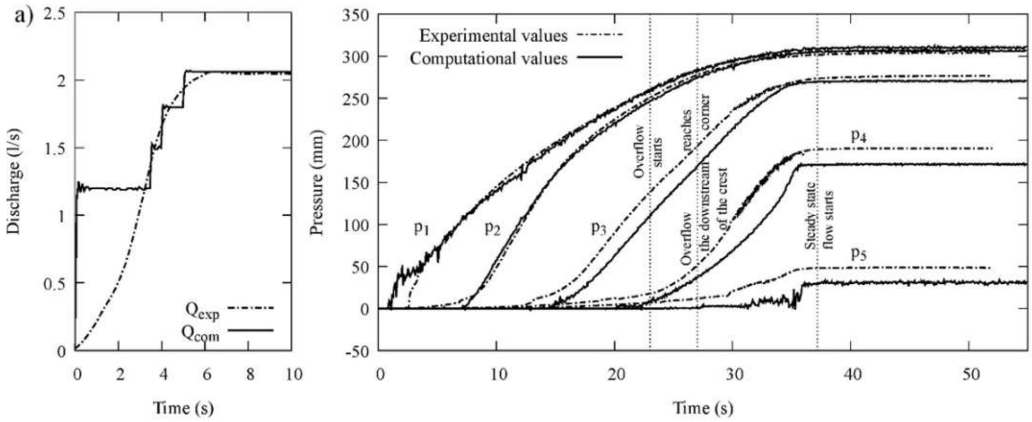


*Figure 42: Measurement of inlet discharge development (left); experimental and computational seepage (right)*

**Measurement of free surface elevation and seepage velocity**

At the same time, a camera was used to record the development of the free surface and the phreatic surface. This serves to contextualise and interpret the measurement results for the bottom pressure with the seepage flow and the overflow. The free surface compared to the computational free surfaces are shown in Figure 42. The free surfaces are similar to the experimental pressures.

At 10.14s, 20.27s and 30.41s the seepage shows a strong curvature at the interface of the porous media which is caused by the surface tension. When the seepage propagates downstream inside the embankment it rises due to the capillarity of the media. As the water reaches the height of the crest, the overflow starts. In general, the pressure measurements obtained from experiments and simulations do not align perfectly in the graph. Nonetheless, the experimental data consistently exceed the computational results. Despite this discrepancy, both datasets exhibit similar trends at corresponding points.

**Comparison Bottom Pressure and Surface Elevation**

During the experiment, air began to become trapped inside the embankment as the overflow was separated from the seepage flow, and the volume of air increased as the water level rose above the top of the dam. The surface tension caused air to become trapped in the pores, which altered the pressure measurements and caused pressure differences at positions p3 to p5 in Figure 43.

The capillary effects in the experiment occurred when the seepage front reached a certain point, intensified as the water level rose and disappeared after the seepage surface met the overflow.

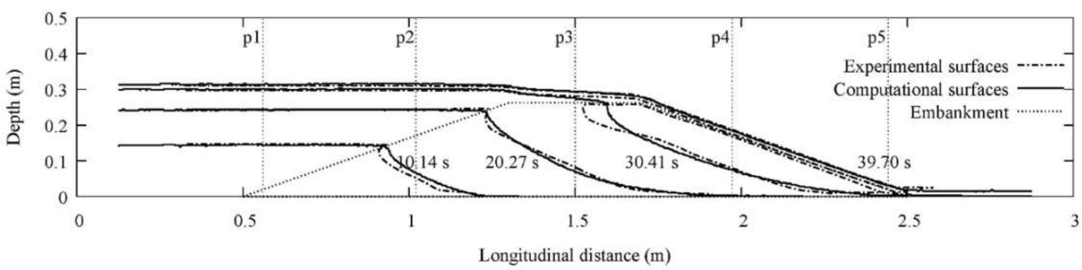


*Figure 43: Experimental and computational surface elevation*

**Interpretation of results**

Several factors can contribute to discrepancies in the measured values. Variations in material-related parameters between the experiment and the model could introduce errors. These deviations will be analysed and addressed in the following discussions to explore potential improvements.

**Free surface elevation and seepage velocity**

The approach for calculating the free surface in the numerical model can be a potential source of error. Therefore, a new approach is used in the model that can eliminate this aspect as a source of error. Furthermore, surface tension and capillarity are not taken into account in the numerical model. These two effects influence the development and position of the free surface and the phreatic surface. This can be another reason for differences in the model and the experiments. According to Körner et al., 2005, these parameters can be considered in the model via the free surface boundary conditions.

**Permeability**

In addition to the discharge, the permeability is a relevant parameter that can be varied within the experiments. Depending on how high the permeability of the material is, the flow behaviour in and over the embankment changes. By specifying the PPI number for the foam used as the dike body, only a rough conclusion can be drawn about the permeability. The permeability decreases with an increasing PPI number, as the pore size decreases with an increasing number of pores over the same distance, resulting in greater resistance to seepage. As in Dietrich et al., 2009, the permeability value should be determined in laboratory experiments. Based on the values obtained from the laboratory experiments, the numerical model can be adjusted to align the permeability, ensuring that the behavior in both the model and the experiment are comparable.

**Inlet Condition**

Exactly the same inlet condition for both the model and the experiment should improve the results for the measuring points p3 to p5. To achieve this, an attempt should be made to open the flume as evenly as possible to 2.0 l/s.

**Bottom layer boundary**

At all measuring points, the pressure rises earlier than in the modelling because there is a sheet flow between the bottom layer and the embankment. Within the modelling, it is assumed that the bottom layer is impermeable. In the experiment, however, the transition between the embankment and the subsoil is not completely impermeable, which leads to the premature increase in bottom pressure. In order to prevent a preferential sheet flow at the bottom boundary a type of floor seal should be installed.

# APPENDIX B: Analysis PIV

In the following the methods to analyse PIV measurements are presented. The first method is called cross- correlation and the second uses a python package including different algorithm to detect particle movement.

## Cross correlation

In order to analyse the recorded image data, the entire recorded area is divided into subareas known as "interrogation windows". The movement vector of the tracer particles is determined using the statistical method "cross- correlation". In Figure 44 the interrogation window 1 (green) is defined in which the particles are localised. The interrogation window 2 (blue) is slightly larger, and the objects are searched for again. A localisation mask is generated from image A, which is placed on the image in order to recognise the correlation between the objects. (Cours INSA, n.d)

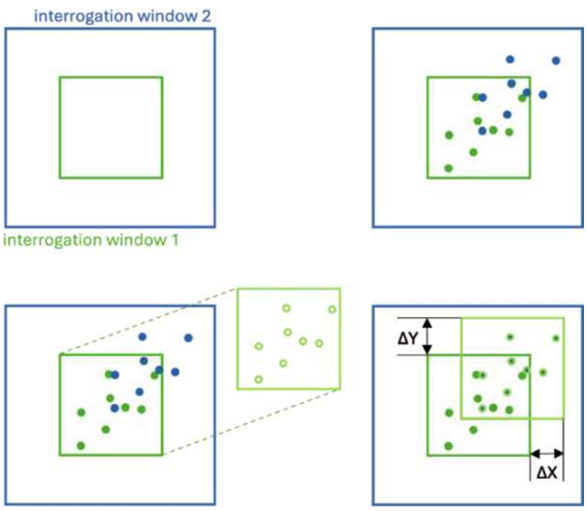


*Figure 44: Interrogation window 1 and 2 to localise particles (based on Cours INSA, n.d)*

Consequently, a movement between the successively captured images can be recognised. The movement vector contains displacements in x and y direction (pixels). Since the time interval between the images is known, the pixel displacement per time interval can be determined, which corresponds to the speed of the particles. A scaling can be carried out afterwards so that the actual velocity of the flow is known. This evaluation is repeated for all interrogation windows, resulting in a velocity field for the entire area. (Cours INSA, n.d.; Raffel et al., 2018)

## OPYFLOW

The python package "OPYFLOW" is used to analyse the velocity fields. In this package, two algorithms are used to recognise the particles in the first step and to detect the movement of the particles in the second step.

### Preprocessing

The working and folder structure is defined at the beginning. All necessary python packages are loaded (opyflow, opencv, maltplotlib etc). The input for the image data can be either a frame sequence or a video. When importing the image data, the region of interest can be defined directly. This allows us to define the area which is calculated to avoid being distracted by lateral or irrelevant objects. The processing plan is defined in the first step of preprocessing. Among other things, this determines from which image the analysis starts and how many image pairs are analysed. The parameters to be defined can be found in Table 4 below.

*Table 4: Parameters to define in the preprocessing with OPYFLOW*

| **Parameter** | **Feature** |
|---|---|
| Ntot | The number of image pairs |
| Shift | The shift between two image pairs |
| Step | The number of images between images in an image pair; If the step becomes larger, the shifts that are recognised become larger. |
| Starting frame | The first frame from which the image pairs are analysed |

After the processing plan has been defined, object detection follows with the Good Features To Track algorithm developed and described by Shi & Tomasi, 1994. This algorithm detects corners of objects with the following function (9).

$$R = \min(\lambda_1, \lambda_2) \tag{9}$$

If $\boldsymbol{\lambda_1}$ and $\boldsymbol{\lambda_2}$ are greater than a threshold value, it is assumed that there is a corner at that location. In "opencv", a number N of strongest corners in quality is found using the Shi-Tomasi algorithm. The number of corners to be found can be specified. Furthermore, the quality level between 0 and 1, which the corner must have as a minimum, can be specified. Corners with a quality level below this are not considered. If the minimum distance between the corners has been specified, the strongest corners can be determined. (OpenCV, 2024c)

### Velocity Processing

The optical flow is used to calculate the movement of the particles that were recognised in preprocessing. Optical flow is the pattern between the apparent movement of objects on a camera between two frames. A 2D vector field is showing movement between points from 1st to 2nd frame (see Figure 45).

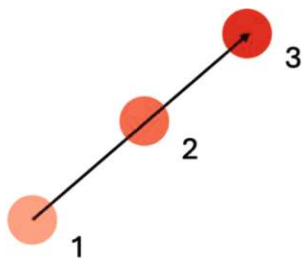


*Figure 45: Vector showing the movement of particles from the 1st to 2nd frame (based on(OpenCV, 2024b) )*

The following assumptions are made to determine the optical flow. The number of pixels between two frames does not change. Furthermore, it is assumed that neighbouring pixels have a similar movement.

In 1st Frame: $I(x, y, t)$

In 2nd frame: $I(x, y, t) = I(x + d, x + dy, t + dt)$

Optical flow equation:

$$f_x u + f_y v + f_t = 0 \tag{1}$$

$$f_x = \frac{\partial f}{\partial x}; f_y = \frac{\partial f}{\partial y} \; with\; f_x, f_y\text{: Image gradients}$$

$$u = \frac{d_x}{dt}; v = \frac{d_y}{dt}$$

$$with\; f_x, f_y\text{: Image gradients}$$

$$f_{t:}\text{Gradient along time}$$

The velocities u and v are initially unknown. Their estimation can be achieved using the Lukas-Kanade algorithm. This algorithm operates on the principle that neighboring pixels exhibit similar motion. Specifically, it assumes that the movement within a 3×3×3 pixel neighborhood around a given point is uniform. This assumption leads to a system of nine equations with only two unknowns. The overdetermined system is then solved using the least squares method. (OpenCV, 2024b)

$$\begin{bmatrix} u \\ v \end{bmatrix} = \begin{bmatrix} \sum_i f_{x_i}^2 & \sum_i f_{x_i} f_{y_i} \\ \sum_i f_{x_i} f_{y_i} & \sum_i f_{y_i}^2 \end{bmatrix}^{-1} \begin{bmatrix} -\sum_i f_{x_i} f_{t_i} \\ -\sum_i f_{y_i} f_{t_i} \end{bmatrix} \tag{2}$$

To determine the optical flow, the algorithm requires the input of the specific points to be tracked, and it will subsequently compute the corresponding flow vectors for these points. The challenge arises when dealing with large movements, as the algorithm primarily addresses small movements. To accommodate large movements, image pyramids are employed. An image pyramid is a hierarchical structure consisting of multiple levels, each representing the same scene at different scales of resolution. At the higher levels, which have lower resolution, large movements are represented as smaller displacements, making them easier to track. Conversely, the lower levels, with higher resolution, capture finer details and smaller movements. This multi-scale approach allows the algorithm to first handle large movements on coarser levels and then refine the results on finer levels. The KLT (Kanade-Lucas-Tomasi) method is advantageous due to its robustness against image noise and minor disturbances, but it is not suited for dense flow estimation. (OpenCV, 2024b)

After the first run, the initial parameters can be adjusted iteratively to achieve optimised results. On the one hand, information about the velocity should be available over the entire range. On the other hand, the velocity height and profiles should be plausible in comparison to the expected values. Some filters and their functions that are available for this are listed here.

### Postprocessing and Interpolation

In the final step, an interpolation process is applied to obtain a complete velocity field. This involves using data from isolated points where the velocity has been accurately measured. The interpolation fills in gaps in areas where the image quality was insufficient or where the number of seed particles was too low to produce reliable measurements. Before the interpolation process, the velocity vectors are subjected to two filters to detect potential outliers. The first filter recognises and suppresses isolated points, while the second filter detects outliers by comparing them with the locally averaged velocity. A Gaussian scheme is used for interpolation. This method can then be used to reproduce the velocity field between two images. The most important and used available filters are collected and described in Table 5. (G. P. D. M. Rousseau, 2019)

*Table 5: Available filters for producing optimized results in OPYFLOW (all available filters can be found here* OpenCV, 2024a)

| **Parameters** | **Features** |
|---|---|
| Norm velocities | |
| *Min/max velocities* | This limits the velocities upwards and downwards. This setting is very closely linked to "step" from the processing plan, as "step" determines the size of the shifts. This means that the larger the step, the larger the shifts that are perceived. |
| Filter | |
| *wayBackGoodFlag* | Specifies the accepted distance between the initial position of the particle and the new position, which is calculated based on the displacement. The calculation is first performed from a to b and then from b to a. |
| *CLAHE* | This increases the local contrasts. TRUE/ FALSE can be set. |
| *RadiusF and maxDevinRad* | The deviation that is expected within radiusF is specified. The deviation is calculated as (x - mean(S)) / std(S), where S is the velocity value within RadiusF and x is the value to be checked. If Dev > maxDev, the value is cancelled. |
| GoodFeaturesToTrack | |
| *qualityLevel* | Parameter that characterises the minimum accepted quality of image corners. The parameter value is multiplied by the best quality measure for the corners, i.e. by the minimum eigenvalue (see cornerMinEigenVal ) or the Harris function response (see cornerHarris ). The corners whose quality measure is smaller than the product are discarded. If, for example, the best corner has the quality measure = 1500 and the qualityLevel=0.01, then all corners with a quality measure of less than 15 are rejected. |
| *maxCorners* | Maximum number of corners to be returned. If there are more corners than are found, the largest of them is returned. maxCorners <= 0 means that no limit is set for the maximum and all corners found are returned. |

| | |
|---|---|
| *minDistance* | Smallest possible Euclidean distance between the returned corners. |
| Optical Flow | |
| *winSize* | Size of the search window at **'each'** pyramid level. |
| *maxLevel* | 0-based maximal pyramid level number; if set to 0, pyramids are not used (single level), if set to 1, two levels are used, and so on. |

# APPENDIX C: Experimental set up and measuring technique for the estimation of the permeability

## Experimental setup and execution of preliminary study

For the steady-state pressure drop measurements, the same experimental setup as in the study by Cocci et al. was used. This setup was integrated into a narrow hydraulic flume. The exact functionality of the recirculating system is described in chapter 5. A schematic of the setup is shown in Figure 46. The flow rate is manually controlled by a valve, and the outflow is managed by three sequentially arranged valves and a trumpet-shaped overflow pipe. Water flows into the flume from the left side and passes through the test body with dimensions of 5x15x10.3 cm (see Figure 47).

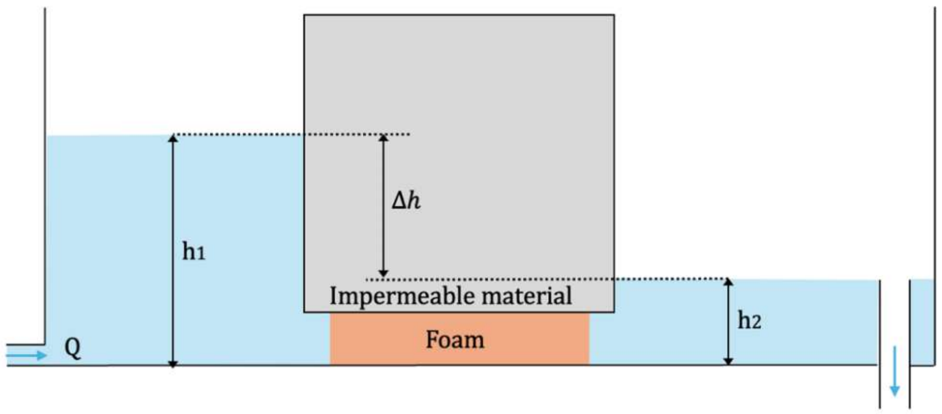


*Figure 46: Experimental setup for the preliminary study to obtain the permeability of the foam*

The experimental setup includes a test body composed of two polyurethane (PUR) filter materials with different permeabilities, as indicated by their PPI ratings provided by the manufacturer. The materials used in the pressure drop measurements are PPI60 and PPI45. An impermeable block is placed above the test body to ensure that water flows exclusively through the test bodies. The objective of the experiment is to measure the water depths on both sides of the test body. By correlating the difference in water heights with the flow rate, the permeability of the materials can be determined.

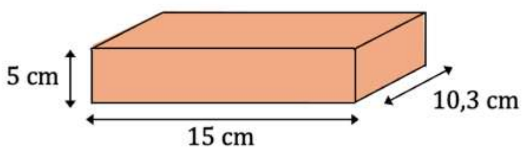


*Figure 47: Dimensions of foam test body*

The water height h1 varies depending on the flow rate. The outflow is fixed by the height of the overflow, which is positioned above the test body. During the experiment, the flow rate is gradually increased from 0.3 l/s to 0.7 l/s. For flow rates below 0.3 l/s, the overflow height is not reached. For flow rates above 0.7 l/s, water accumulates so strongly upstream that the setup floods.

After setting a new flow rate, one must wait until the water level stabilizes. As this is a steady-state experiment, the water level must remain constant throughout the measurement period. Even minimal pressure fluctuations can significantly impact the measurements. All data are recorded in Table 8 and Table 9. The filtration velocity, or the averaged flow velocity through the porous medium, can be determined using the cross-sectional geometry, pressure head, and flow rate. The flow rate can be controlled and measured with a flow meter positioned at the inlet.

$$Q = h \cdot b \cdot u = h_1 \cdot b \cdot u_1 = h_2 \cdot b \cdot u_2 = const. \quad (3)$$

The mass conservation equation (3) refers to the entire cross-sectional area of the filter, allowing the flow velocity through the filter's pore space to be determined.

**Experimental procedure and methodology**

The following section outlines the technique regarding the determination of the permeability of the filter foam, based on the studies by Dietrich et al., 2009 and Cocci, 2021.

A filter foam is employed for the embankment body, characterized solely by its pores per inch (PPI) value. A higher PPI indicates a greater number of pores in the material; however, this does not directly reveal the material's permeability. Permeability is crucial for evaluating how different materials affect the flow through and over the embankment. Furthermore, to ensure consistency between the model and the experiment, it is essential to use identical parameters, which can only be achieved if all relevant parameters and their values are known.

A quadratic equation is used to describe the relationship between the flow velocity and the pressure drop as the material is highly permeable. The linear part of the fit function is related to the dynamic viscosity $\eta$ and the quadratic part to the density of air $\rho$, so that the two permeability coefficients $K_1$ and $K_2$ can be determined. This fit function is also known as the Darcy-Forchheimer equation (4). (Dietrich et al., 2009)

Decreasing porosity means an increase in solid material in the same volume, which results in increased flow resistance. The quadratic term in equation (4) is more sensitive to the pressure drop. The same tests were performed with different materials, and upon comparison of the results, no material-specific effects were observed.

$$\frac{\Delta p}{\Delta L} = \frac{\eta}{K_1} \cdot u + \frac{\rho}{K_2} \cdot u^2 \quad (4)$$

The experiments were carried out for different metallic materials and the fitting curves of each material were compared. For all materials, the same behaviour can be detected regarding the pressure drop if the porosity and PPI number are the same. A dimensionless comparison of the materials is possible if the Hagen and Reynolds (see equation (5)) numbers are determined from the results. Regardless of which material and which specific properties, they all correlate on one line (see Figure 48). It can be concluded that the sponges are geometrically the same. (Dietrich et al., 2009)

$$\mathrm{Hg} = \frac{\Delta p}{\Delta L} \cdot \frac{d_\mathrm{h}^3}{\rho \cdot \nu^2} \, and \, \mathrm{Re} = \frac{u \cdot d_\mathrm{h}}{\psi \cdot \nu} \tag{5}$$

With the hydraulic diameter $d_\mathrm{h}$:

$$\begin{aligned} d_\mathrm{h} &= 4 \cdot \frac{\text{cross section available for flow}}{\text{wetted perimeter}} \\ &= 4 \cdot \frac{A_\mathrm{fluid}}{U} \cdot \frac{L}{L} = 4 \cdot \frac{V_\mathrm{fluid}}{S} \cdot \frac{V}{V} = 4 \frac{\psi}{S_\mathrm{v}} \end{aligned} \tag{6}$$

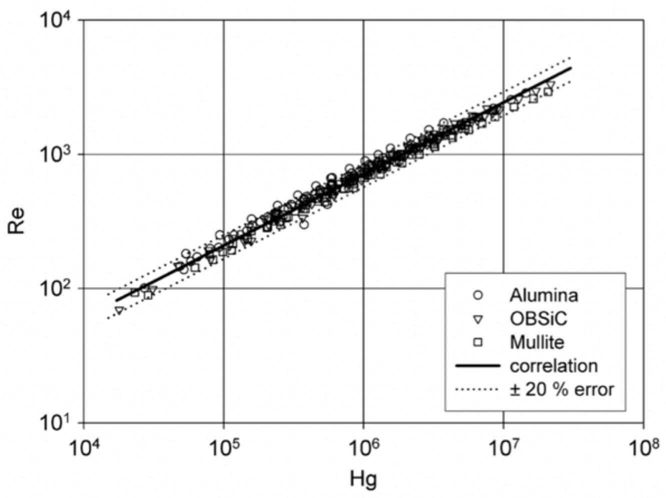


*Figure 48: The dimensionless air velocity (Reynolds number) is compared with the dimensionless pressure drop (Hagen number) for alumin, mullite, and OBSiC sponges (*Dietrich et al., 2009*)*

Cocci, 2021 has developed the tests of Dietrich et al. 2009 for ceramic sponges further and transferred them to the determination of the permeability of filter materials made of PUR. His results for the permeability of the filters agree with the values available from the data sheets for the material. Cocci uses the Darcy-Forchheimer formula (see equation (5)) to determine the permeability.

In the study by Cocci, 2021 a polynomial fitting function is used to calculate the permeability from the measured values. When $f(u) = \Delta h / \Delta L$, with $\Delta p = \rho \cdot g \cdot \Delta h$, the coefficients A and B can be calculated as follows. C represents the inertial loss term, which is often negligibly small and will therefore not be further considered in this discussion. (Bischelmaier, 2011)

Fit function:

$$f(u) = A \cdot u^2 + B \cdot u + C \tag{7}$$

Coefficients A und B:

$$A = \frac{1}{g \cdot K_2}\ ;\ B = \frac{\nu}{g \cdot K_1} \tag{8}$$

By measuring the difference in pressure head between upstream and downstream, the pressure drop can be determined. From this, the flow velocity can be derived. The experiments are detailed in the chapter 2.3.4. The variables A and B from equation (8) are calculated using Excel's RGP function. This way the two parameters $K_1$ and $K_2$ of the permeability can be obtained. Here, the coefficient A corresponds to the kinetic resistance, while B represents the viscous resistance. $K_1$ represents the permeability according to Darcy's law, and $K_2$ accounts for the kinetic resistance in turbulent flow. (Dietrich et al., 2009)

Dietrich et al., 2009 calculate the parameters A and B for various materials and take the mean value. The pressure drop in solid sponges can also be calculated by using the Ergun formula (6), derived from the definition of the friction factor. By comparing the Darcy-Forchheimer equation with the Ergun formula the values for the parameters A and B can be determined. The results are $A$ = 110 and $B$ = 1.45. Using these averaged values, a geometry- and material-independent fit for all experimental data can be established. By comparing the Darcy-Forchheimer equation (5) with the Ergun equation (9) using the provided values for the parameter A and B a formula for calculating the hydraulic diameter is provided. (Cocci, 2021; Dietrich et al., 2009)

Ergun formulae with parameters A and B:

$$\frac{\Delta p}{\Delta L} = 110 \cdot \frac{\mu}{\psi \cdot d_{\mathrm{h}}^2} \cdot u + 1.45 \cdot \frac{\rho}{\psi^2 \cdot d_{\mathrm{h}}} \cdot u^2 \tag{9}$$

Hydraulic diameter:

$$d_{\mathrm{h}} = \sqrt{\frac{110 \cdot K_1}{\psi}} \tag{10}$$

Furthermore a linear relationship between the calculated hydraulic diameters for different materials and the correlating PPI numbers can be drawn. This correlation can be modeled using an empirical formula (8) that allows the calculation of the hydraulic diameter based on the manufacturer's specified PPI number. This formula is applicable to all foams with a constant porosity of 80%. (Cocci, 2021; Dietrich et al., 2009)

$$d_{\mathrm{h}} = 0{,}028\ (\mathrm{m}) \cdot ppi^{-0{,}721} \tag{11}$$

**Results**

The results of the preliminary study are presented in the following chapter. The aim here was to determine the permeabilities of the two different permeable filter materials used for the embankment by conducting experiments. In order to determine the Reynolds and Hagen number for a dimensionless comparison of the pressure drop measures given by the foam company and the values measured experimentally, the hydraulic diameter is needed. Two different approaches for its determination are presented in the results.

**Permeability**

Using the RGP function in Excel, the coefficients A and B can be calculated (as per equation (8)). The resulting permeabilities for the materials PPI 45 and PPI 60 are summarized in Table 6. Additionally, permeability values for PPI 45 were available from a product datasheet and are included for comparison. It can be observed that the measured and provided values for $K_1$ for PPI 45 are consistent. Since the same measurement and calculation methods were applied to PPI 60, it is assumed that the derived permeability values are also representative for this material.

*Table 6: Permeabilities for PPI 45 and PPI60*

| | PPI45 | PPI60 |
|---|---|---|
| PPI | 45 | 60 |
| K1 | -1,53E-09 | 1,31E-14 |

**Hydraulic Diameter**

The porosity was determined using the specific weight given in the data sheet. For this purpose, the volume and weight of a test body were determined, set in relation and the pore volume $V_e$ calculated from this. The porosity $\psi$ can then be determined using the equation (13) and the results can be seen in Table 7.

$$\psi = \frac{V_e}{V_{ges}} \tag{13}$$

The filter material is heterogeneous and due to this irregularity an analytical determination of the hydraulic diameter is not possible. Dietrich et al., 2009 developed an empirical formula that allows the hydraulic diameter to be calculated solely based on the PPI number. Dietrich et al., 2009 use materials with a porosity of 80%. The materials used here have a porosity between 68% and 70%, so the formula can only be used as an approximation.

$$d_\mathrm{h} = 0{,}028\ (\mathrm{m}) \cdot \mathrm{PPI}^{-0{,}721} \tag{14}$$

If the pressure gradient for the material is known, the hydraulic diameter can also be calculated independently of the geometry. Dietrich et al., 2009 determined two material-independent parameters and, by comparing the Darcy-Forchheimer equation with the Ergun equation, provided another formula for calculating the hydraulic diameter:

$$d_\mathrm{h} = \sqrt{\frac{110 \cdot K_1}{\psi}} \tag{15}$$

The results for both approaches are summarized in the following Table 7. To calculate the permeability, the empirically determined hydraulic diameter was used.

*Table 7: Hydraulic diameter for different PPI numbers*

| | PPI45 | PPI60 |
|---|---|---|
| PPI | 45 | 60 |
| dh in mm (equation (14)) | 0,1800 | 0,1463 |
| dh in mm (equation (15)) | 0,7249 | 0,0022 |
| porosity | 32% | 31% |

**Re- Hg diagram**

Permeability tests for both materials found in the literature use air as the fluid. To compare the measurements across different flow media, dimensionless numbers are used. From the flow velocity and the pressure gradient, the Reynolds and Hagen numbers are determined (see equation (17) and (18)). For experiments using water as the flow medium, the pressure gradient was converted into meters of water column per meter length.

For PPI 60, only datasheets for the permeability of the material polyester were available (ISP GmbH, 2024c). For PPI 45, the permeability data for both materials (polyester and polyether) were available, allowing for a comparison to investigate whether different materials with the same PPI number have the same permeability. This comparison can be found in Appendix A. It was determined that the permeabilities of polyester and polyether differ significantly. As a result, there is no datasheet information regarding the permeability for PPI 60. It is assumed that if the measured and given permeabilities for PPI 45 match, as demonstrated through a dimensionless comparison using the Reynolds-Hagen diagram (seen Figure 48), the experimentally measured values for PPI 60 can be assumed as accurate.

With:

$$\Delta p = \rho \cdot g \cdot \Delta h \tag{16}$$

Results in:

$$\mathrm{Re} = \frac{u \cdot d_\mathrm{h}}{\psi \cdot \nu} \tag{17}$$

$$\mathrm{Hg} = \frac{\Delta h}{\Delta L} \cdot \frac{g \cdot d_\mathrm{h}^3}{\nu^2} \tag{18}$$

The water temperature during the experiment was assumed to be 20°C. Hence, the water density was $\rho = 998.2\ \mathrm{kg/m^3}$, and the kinematic viscosity was $\nu = 1.004 \cdot 10^{-6}\ \mathrm{m^2/s}$ (Cocci, 2021). The hydraulic diameter calculated is used for the dimensionless comparison of the measured and given permeability values of the material. The Re-Hg relationship for PPI45 from the datasheets and the experiments is presented in Figure 49. The datasheets provide the pressure drop for an airflow, assuming an air density of $\rho = 1.205\ \mathrm{kg/m^3}$ and a kinematic viscosity of $\nu = 1.51 \cdot 10^{-5}\ \mathrm{m^2/s}$ (Cocci, 2021). The Re- Hg diagram shows the measured values for PPI 45 with a filter mat thickness of 5cm. The Reynolds and Hagen numbers of 40mm, 60mm and 80mm are shown from the data sheet.

The measured values and the values from the data sheet are in the same range. The hydraulic radii for the product data sheets are not known and the empirically determined hydraulic radius calculated with equation (14) was used for both (experiment and data sheet) in order to calculate the respective Reynolds and Hagen numbers.

Appendix A contains additional results from the preliminary study. It includes a comparison between PUR (polyurethane) based on polyester and polyether for PPI 45, as well as a plot of the pressure drop relative to velocity for both materials.

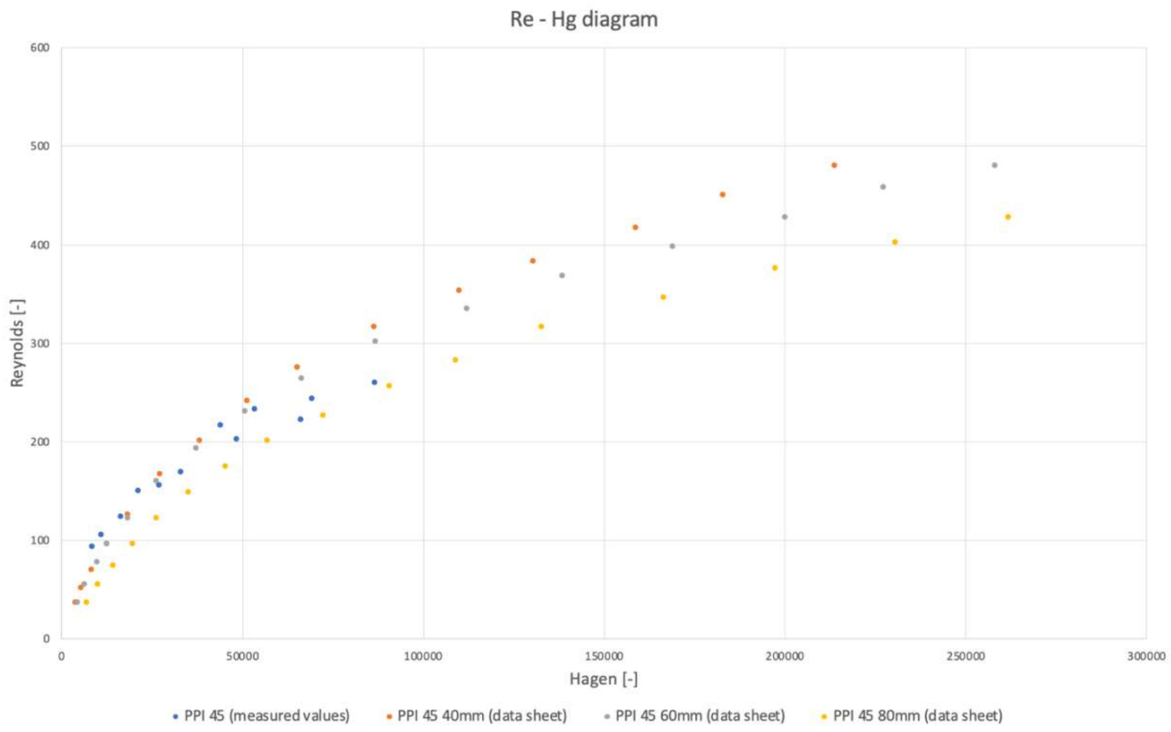


*Figure 49: Re – Hg diagram for PPI45 (ISP GmbH, 2024b)*

# APPENDIX D: Additional results for pressure drop measurements

## Manufacturers data sheets (PPI45 and PPI 60)

Industrie-Schaum-Produkte

**TECHNISCHES DATENBLATT**

**- ISP-Filterschaum PPI 45 -**

| | |
|---|---|
| ***Qualität:*** | ISP-Filterschaum PPI 45 |
| ***Rohstoffbasis:*** | Polyurethan auf Polyesterbasis |
| ***Struktur:*** | total offenporig |
| ***Porenzahl:*** | 45 Poren per 1 Inch ± 7 Poren |
| ***Spezifisches Gewicht:*** (DIN EN ISO 845) | 29 – 35 kg/m³ |
| ***Zugfestigkeit:*** (DIN EN ISO 1798) | mind. 130 kPa |
| ***Bruchdehnung:*** (DIN EN ISO 1798) | mind. 110 % |
| ***Stauchhärte bei 40 % Kompression:*** (DIN EN ISO 3386-1) | 3,0 – 5,5 kPa |
| ***Temperaturgrenze:*** | - 40° C bis + 100° C |
| ***Ausscheidungsfrei:*** | ja |
| ***Lieferbare Farben:*** | Standard: dunkel<br>andere Farben auf Wunsch |
| ***Lieferbare Formen:*** | Blöcke 2.000 x 1.000 mm<br>Höhe ca. 580 mm<br>Platten ab 2 mm Dicke<br>Zuschnitte, Streifen, Stanzteile |
| ***Anwendungsgebiete:*** | Luftfilter,<br>verdichtet auch als<br>Geräuschfilter u.a. |

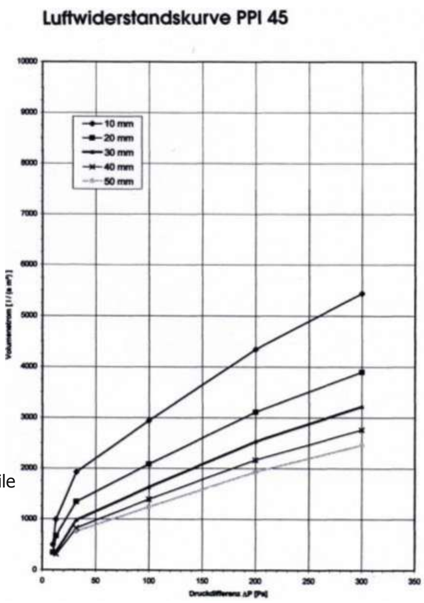


Dieses Merkblatt will Sie beraten. Die hier gemachten Angaben entsprechen unserem besten Wissen. Eine Verbindlichkeit kann daraus jedoch nicht abgeleitet werden.

0901/16

ISP GmbH & Co. KG, Hoenbergstraße 13, 65555 Limburg, Germany
Tel. +49 (0) 64 31 / 52 99-0 Fax: +49 (0) 64 31 / 52 99-33
www.isp-schaum.de info@isp-schaum.de

*Figure 50: Data sheet PPI 45 (ISP GmbH, 2024b)*

Industrie-Schaum-Produkte

## TECHNISCHES DATENBLATT

### - ISP-Filterschaum PPI 60 -

| | |
|---|---|
| ***Qualität:*** | ISP-Filterschaum PPI 60 |
| ***Rohstoffbasis:*** | Polyurethan auf Polyesterbasis |
| ***Struktur:*** | total offenporig |
| ***Porenzahl:*** | 60 Poren per 1 Inch<br>(min. 55 PPI – max. 70 PPI) |
| ***Spezifisches Gewicht:***<br>(DIN EN ISO 845) | 27 – 33 kg/m³ |
| ***Zugfestigkeit:***<br>(DIN EN ISO 1798) | mind. 220 kPa |
| ***Bruchdehnung:***<br>(DIN EN ISO 1798) | mind. 220 % |
| ***Stauchhärte bei 40 % Kompression:***<br>(DIN EN ISO 3386-1) | 2,0 – 4,0 kPa |
| ***Temperaturgrenze:*** | - 40° C bis + 100° C |
| ***Ausscheidungsfrei:*** | ja |
| ***Lieferbare Farben:*** | Standard: dunkel<br>andere Farben auf Wunsch |
| ***Lieferbare Formen:*** | Blöcke 2.000 x 1.000 mm<br>Höhe ca. 660 mm<br>Platten ab 2 mm Dicke<br>Zuschnitte, Streifen, Stanzteile |
| ***Anwendungsgebiete:*** | Luftfilter,<br>verdichtet auch als<br>Geräuschfilter u.a. |

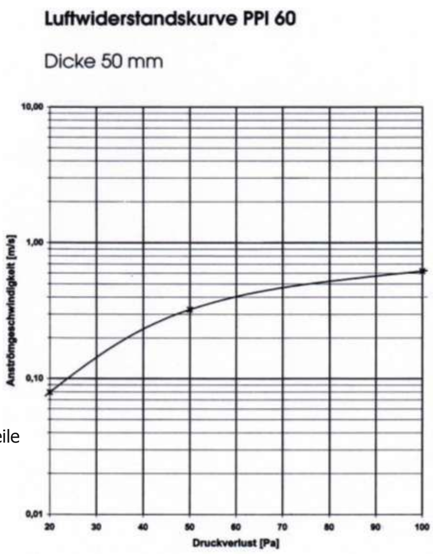


Dieses Merkblatt will Sie beraten. Die hier gemachten Angaben entsprechen unserem besten Wissen.
Eine Verbindlichkeit kann daraus jedoch nicht abgeleitet werden.

0909/16

ISP GmbH & Co. KG, Hoenbergstraße 13, 65555 Limburg, Germany
Tel. +49 (0) 64 31 / 52 99-0 Fax: +49 (0) 64 31 / 52 99-33
www.isp-schaum.de info@isp-schaum.de

*Figure 51: Data sheet PPI 60 (ISP GmbH, 2024c)*

### Measured pressure drop of PPI45 and PPI60

The pressure drop measurements for the materials PPI 45 and PPI 60 were analyzed in relation to the flow velocity (see Figure 52 and Figure 53). The data was fitted using a polynomial function to model the relationship between pressure drop and velocity. A clear trend emerged from the analysis, indicating that higher velocities were achieved with the PPI 45 material for the same pressure drop when compared to the PPI 60 material. This suggests that PPI 45 exhibits a higher permeability, allowing the fluid to pass through the porous medium more easily than in the case of PPI 60. The increased permeability of PPI 45 is consistent with its structural properties, which enable less resistance to flow, thereby resulting in greater flow velocities under similar pressure conditions.

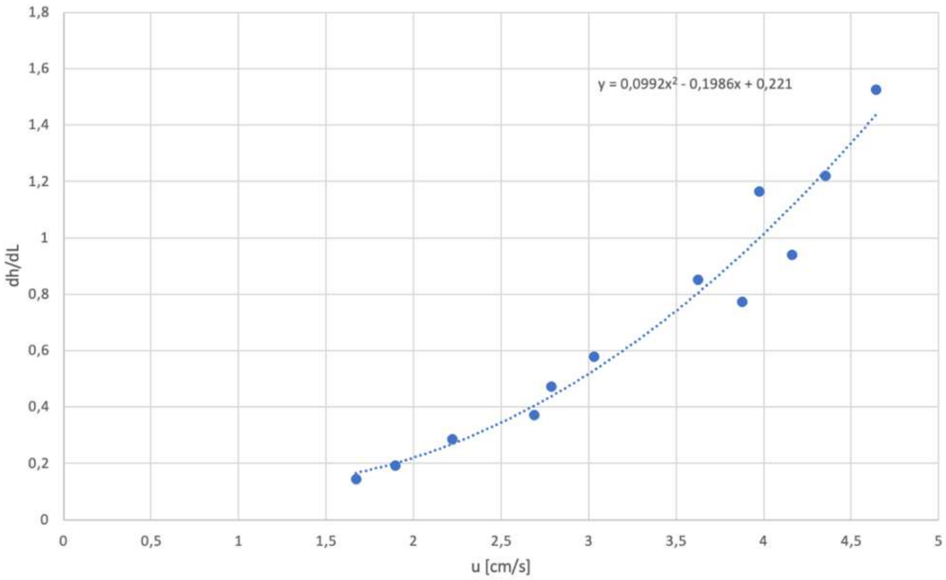


*Figure 52: PPI 45, pressure drop as a function of the velocity*

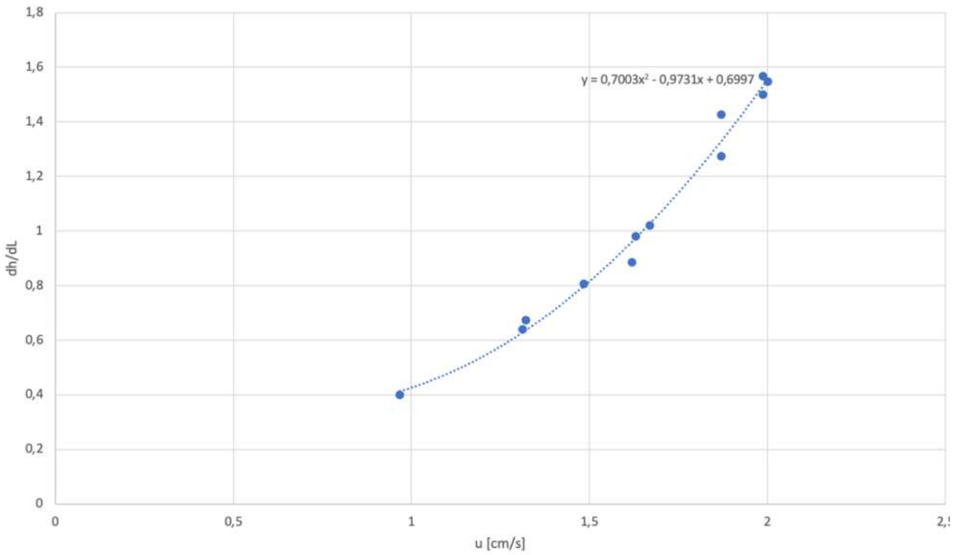


*Figure 53: PPI 60, pressure drop as a function of the velocity*

## Comparison Polyether and Polyester

The comparison between PUR based on polyester and polyether filter materials was focused on examining the flow resistance of these two materials. For the PPI 60 grade, the manufacturer's product data sheets (ISP GmbH, 2024a, 2024c, 2024b) provided information only on the flow resistance and permeability of polyester. Therefore, the behavior of both polyester and polyether materials was analyzed to determine whether the product data for polyester could be used to compare the measured permeability of PPI 60 with the manufacturer's specifications.

The flow resistance values for both polyester and polyether materials with PPI 45 are presented in Figure 54 and Figure 55, with flow resistance measurements taken for different material thicknesses. The results show that, for polyester, significantly higher velocities are achieved at the same pressure drop compared to polyether. The graphical data for polyester indicates that for a pressure drop up to 300 Pa, a maximum velocity of 5.5 m/s was achieved. In contrast, polyether reaches only 1.1 m/s at the same pressure drop of 300 Pa. This indicates that polyester exhibits five times the velocity of polyether, implying a significantly higher permeability in polyester than in polyether under similar conditions.

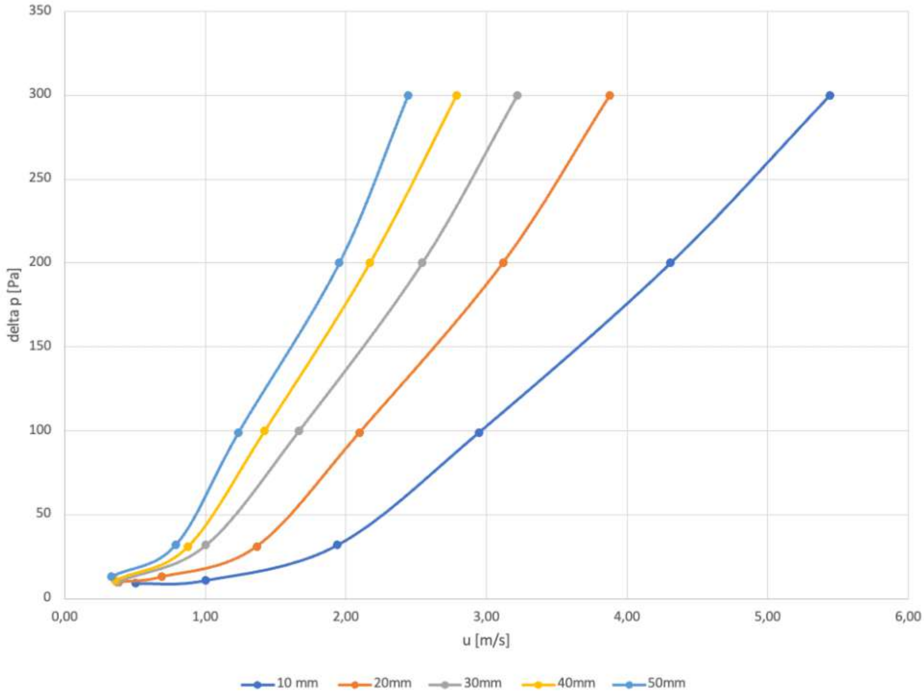


*Figure 54: Flow resistance of PPI 45 Polyester (ISP GmbH, 2024a)*

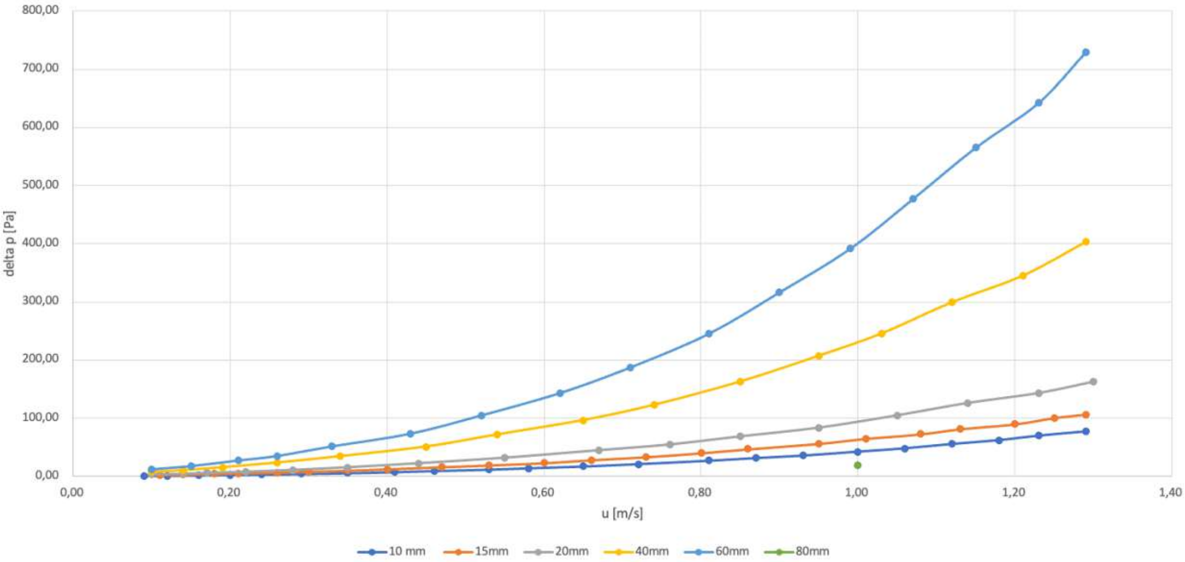


*Figure 55: Flow resistance of PPI 45 Polyether (ISP GmbH, 2024b)*

## Table with measured values and results

*Table 8: Measured values (PPI45, 5cm)*

| h1 | h2 | delta h | Q [cm3/s] | A1 | A2 | u1 [cm/s] | u2 | um | h/L | Re | Hg |
|---|---|---|---|---|---|---|---|---|---|---|---|
| 11,1 | 8,9 | 2,2 | 170 | 114,33 | 91,67 | 1,4869238 | 1,854478 | 1,6707009 | 0,14666667 | 93,585126 | 8319,7146 |
| 11,9 | 9 | 2,9 | 200 | 122,57 | 92,7 | 1,6317206 | 2,1574973 | 1,894609 | 0,19333333 | 106,12744 | 10966,897 |
| 13,5 | 9,2 | 4,3 | 250 | 139,05 | 94,76 | 1,7979144 | 2,638244 | 2,2180792 | 0,28666667 | 124,24679 | 16261,26 |
| 15 | 9,4 | 5,6 | 320 | 154,5 | 96,82 | 2,0711974 | 3,3051023 | 2,6881498 | 0,37333333 | 150,57802 | 21177,455 |
| 16,7 | 9,6 | 7,1 | 350 | 172,01 | 98,88 | 2,0347654 | 3,539644 | 2,7872047 | 0,47333333 | 156,12663 | 26849,988 |
| 18,5 | 9,8 | 8,7 | 400 | 190,55 | 100,94 | 2,0991866 | 3,9627501 | 3,0309684 | 0,58 | 169,78117 | 32900,69 |
| 20,6 | 9 | 11,6 | 500 | 212,18 | 92,7 | 2,3564898 | 5,3937433 | 3,8751165 | 0,77333333 | 217,06654 | 43867,586 |
| 23,2 | 9,1 | 14,1 | 560 | 238,96 | 93,73 | 2,3434884 | 5,9746079 | 4,1590482 | 0,94 | 232,97111 | 53321,807 |
| 28,8 | 10,5 | 18,3 | 690 | 296,64 | 108,15 | 2,3260518 | 6,3800277 | 4,3530398 | 1,22 | 243,83764 | 69204,899 |
| 33,5 | 10,6 | 22,9 | 770 | 345,05 | 109,18 | 2,2315606 | 7,0525737 | 4,6420672 | 1,52666667 | 260,02766 | 86600,666 |
| 22,6 | 9,8 | 12,8 | 510 | 232,78 | 100,94 | 2,1909099 | 5,0525064 | 3,6217082 | 0,85333333 | 202,87175 | 48405,612 |
| 27,5 | 10 | 17,5 | 600 | 283,25 | 103 | 2,1182701 | 5,8252427 | 3,9717564 | 1,16666667 | 222,47987 | 66179,548 |

*Table 9: Measured values (PPI60, 5cm)*

| h1 | h2 | delta h | Q | A1 | A2 | u1 [cm/s] | u2 | um | h/L | Re | Hg |
|---|---|---|---|---|---|---|---|---|---|---|---|
| 14,8 | 8,8 | 6 | 110 | 152,44 | 90,64 | 0,7215954 | 1,2135922 | 0,9675938 | 0,4 | 45,4682934 | 12178,52 |
| 19 | 8,9 | 10,1 | 165 | 195,7 | 91,67 | 0,8431272 | 1,7999345 | 1,3215309 | 0,6733333 | 62,1001848 | 20500,509 |
| 24,4 | 9,1 | 15,3 | 228 | 251,32 | 93,73 | 0,9072099 | 2,4325189 | 1,6698644 | 1,02 | 78,4687597 | 31055,226 |
| 28,4 | 9,3 | 19,1 | 270 | 292,52 | 95,79 | 0,9230138 | 2,8186658 | 1,8708398 | 1,2733333 | 87,9128134 | 38768,289 |
| 30,9 | 9,5 | 21,4 | 280 | 318,27 | 97,85 | 0,8797562 | 2,8615227 | 1,8706395 | 1,4266667 | 87,9033982 | 43436,721 |
| 32 | 9,5 | 22,5 | 300 | 329,6 | 97,85 | 0,9101942 | 3,0659172 | 1,9880557 | 1,5 | 93,4209159 | 45669,45 |
| 33,3 | 9,8 | 23,5 | 310 | 342,99 | 100,94 | 0,9038164 | 3,0711314 | 1,9874739 | 1,5666667 | 93,3935766 | 47699,203 |
| 21,5 | 9,4 | 12,1 | 200 | 221,45 | 96,82 | 0,9031384 | 2,0656889 | 1,4844137 | 0,8066667 | 69,7542244 | 24560,015 |
| 19 | 9,4 | 9,6 | 170 | 195,7 | 96,82 | 0,8686765 | 1,7558356 | 1,3122561 | 0,64 | 61,6643502 | 19485,632 |
| 22,1 | 8,8 | 13,3 | 210 | 227,63 | 90,64 | 0,9225498 | 2,3168579 | 1,6197038 | 0,8866667 | 76,1116577 | 26995,719 |
| 23,5 | 8,8 | 14,7 | 215 | 242,05 | 90,64 | 0,8882462 | 2,3720212 | 1,6301337 | 0,98 | 76,6017693 | 29837,374 |
| 32,2 | 9 | 23,2 | 290 | 331,66 | 92,7 | 0,8743894 | 3,1283711 | 2,0013803 | 1,5466667 | 94,0470518 | 47090,277 |

*Table 10: Results (PPI45, 5cm)*

| $Au^2+Bu+C$ | A | B | C | $K_1$ [cm²] | $K_2$ [cm] |
|---|---|---|---|---|---|
| PPI45 (measured) | 0,425752 | -0,669475 | | -1,5287E-05 | 0,002394279 |
| PPI45 (data sheet) | 0,510761 | -9,510074 | | -1,4256E-05 | 0,001995783 |

| PPI 45 | $K_1$ [m²] | $K_2$ [m] |
|---|---|---|
| measured | -1,5287E-09 | 2,39428E-05 |
| data sheet | -1,4256E-09 | 1,99578E-05 |

*Table 11: Results (PPI60, 5cm)*

| $Au^2+Bu+C$ | A | B | C | $K_1$ [cm²] | $K_2$ [cm] |
|---|---|---|---|---|---|
| PPI60 (measured) | 1,18931121 | -0,8948198 | | -1,14374E-05 | 0,00085711 |

| PPI 60 | $K_1$ [m²] | $K_2$ [m] |
|---|---|---|
| measured | 1,30815E-14 | 8,5711E-06 |

# APPENDIX E: Filter process exemplary for position 1

**Filter process/ iterative determination of parameters exemplary for position 1**

- Is repeated similarly for the following items
- Filtering process is here shown without a mask

**Processing plan (Ntot, Starting frame, step, shift)**

**Ntot**

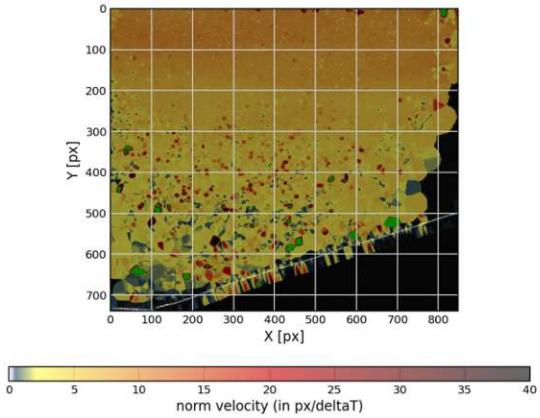


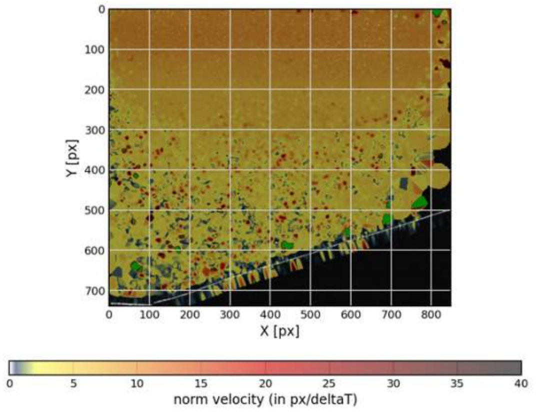


Ntot=20 Ntot = 40

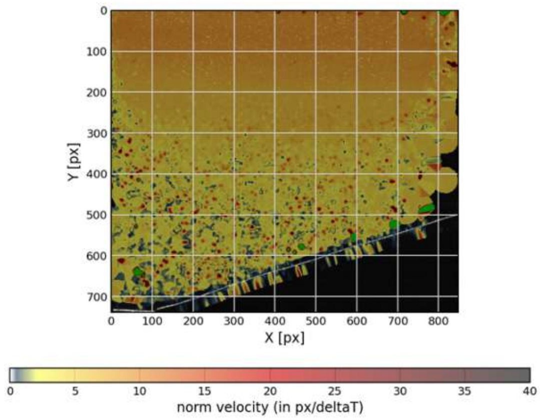


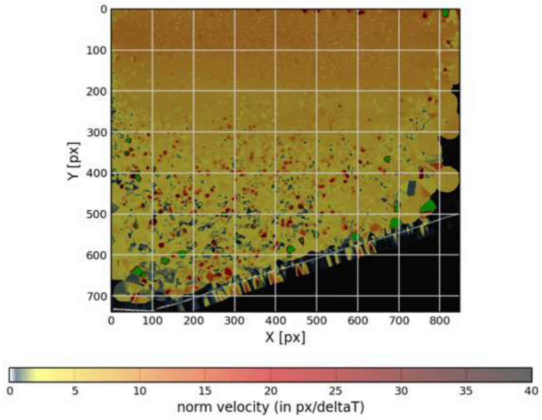


Ntot = 60 Ntot 30

- no difference in the results between 40 and 60
- choose ntot 40 better + starting frame e.g. 15

**Starting frame**

Starting frame=1 Starting frame = 15

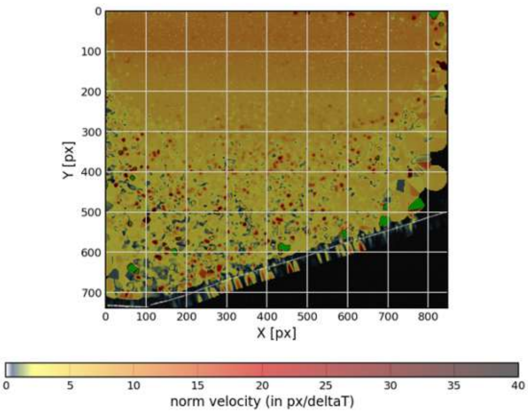


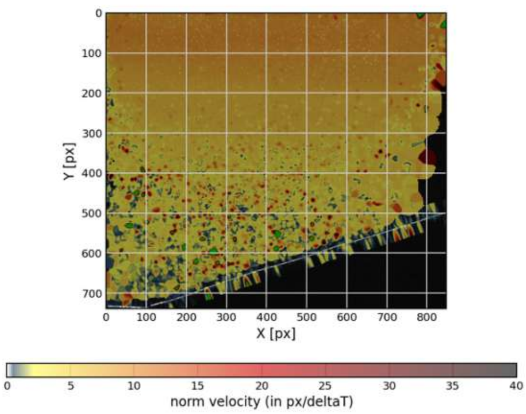


Starting frame 30

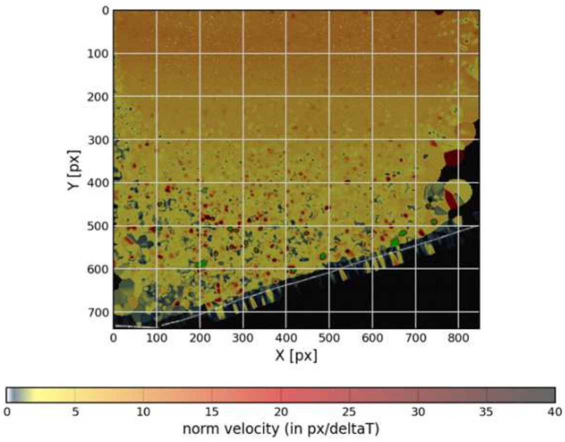


- in the lower right corner of the area, fewer particles are recognisable as the starting frame increases (less speed information)
- remaining information is evenly distributed →starting frame = 1is still used + the region of interest is slightly reduced → 50 pixels are removed at both edges (1.9cm each)

**ROI**

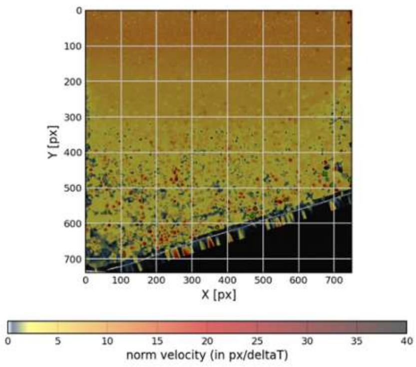


**Velocity (set vlim)**

The minimum + maximum speeds are defined

- to reduce outlier

- plausible velocity is not more than 20px/delta t

Ohne vlim

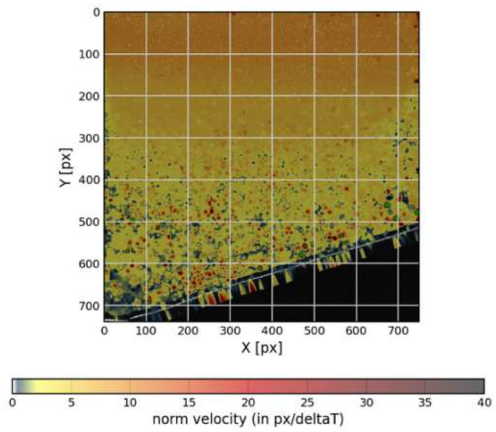


mit vlim (0,2;20)

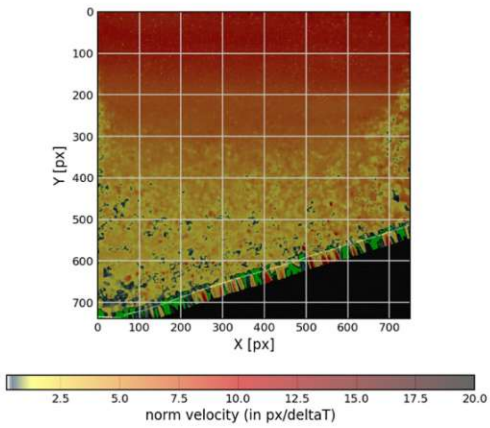


**Filtering (wayBackGoodFlag, CLAHE, RadiusF and maxDevInRadius)**

- To eliminate outliers
- Die geschwindigkeitsbegrenzung ist hier nochmal definiert für Geschwindigkeiten in richtung der x achse
- **wayBackGoodFla**g: Specifies the distance accepted between the initial feature position and the position calculated by using the displacement from A to B and then from B to A (where A and B are the pair on which optical flow is calculated).
- **CLAHE**: Enables Contrast Limited Adaptive Histogram Equalization, which enhances local contrasts. Set it to True to apply the filter.
- **RadiusF and maxDevInRadius**: Specify the maximum deviation expected within RadiusF. Deviation is calculated as (x - mean(S)) / std(S), where S is the velocity values within RadiusF, and x is the value being tested. If Dev > maxDev, the value is deleted.

**wayBackGoodFlag + range vx wie vlim**

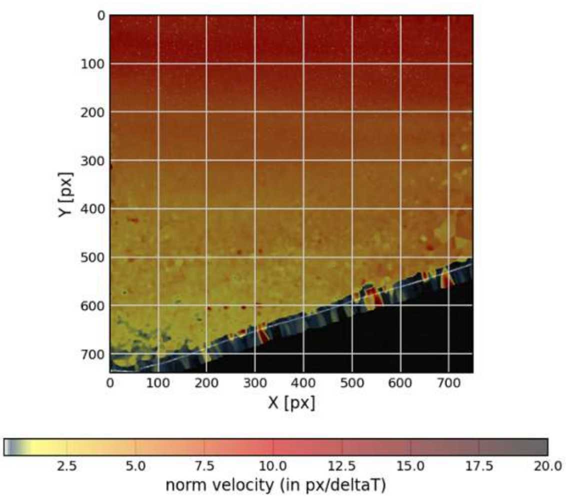


- already looks much better
- by default waygoodflyback: inf (infinite)
- selected waygoodflyback: 3

**RadiusF and maxDevInRadius**

- By default
- RadiusF: 30
- maxDevInRadius: inf

The following parameters are selected:

- RadiusF: 10
- maxDevInRadius: 1

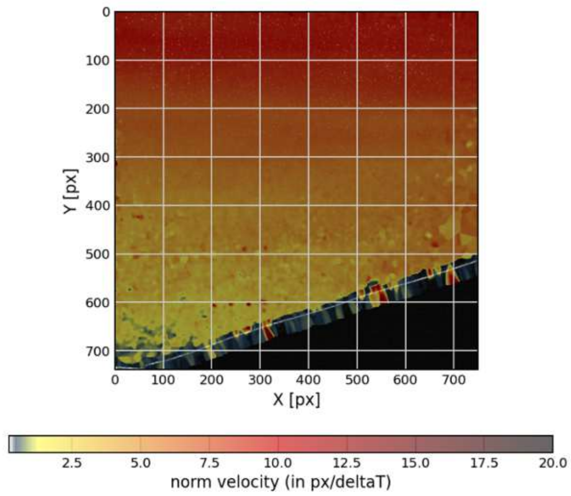


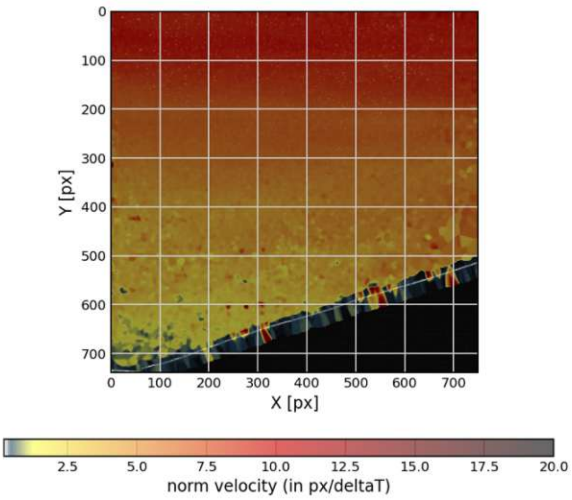


- no big difference visible, but can still be left as it is

**CLAHE**

Set to TRUE

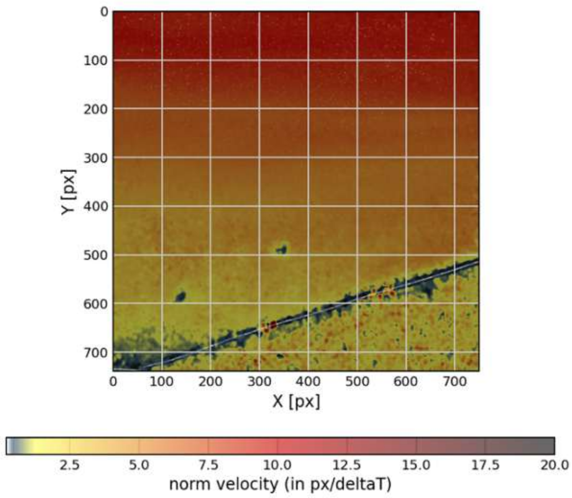


- recognises movements in areas where no particles can be located
- is not used in the further course

**GoodFeaturesToTrack (quality Level)**

**Quality level**

→ set to 0.001 (default: 0.005)

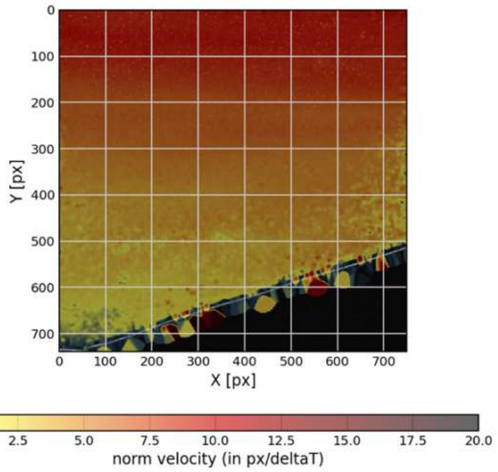


**Postprocessing (SetGridToInterpolateOn)**

- A grid with a grid step of 1 is selected manually, on which the velocities are interpolated
- An even more even distribution of the velocities is expected

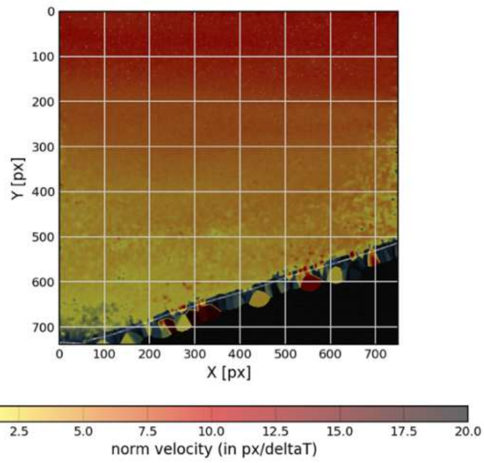


- Interpolation Grid with step=1 → reducing the step makes no difference except that the calculation takes longer/ interpolation because there are more grid points

**<u>Comparison before and after setting processing plan, filtering or post-processsing (without scale, without mask)</u>**

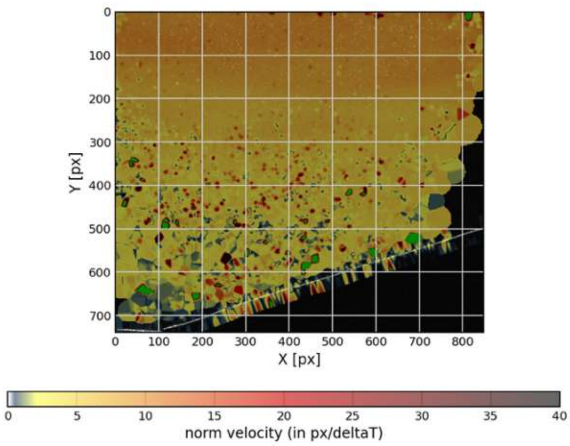


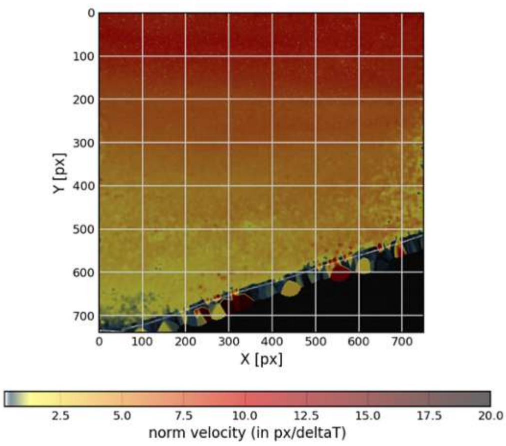

## APPENDIX F: Velocity change in x- and y direction

### Position 1: Velocity change between PPI45 and PPI60 in x- direction (right) and y – direction

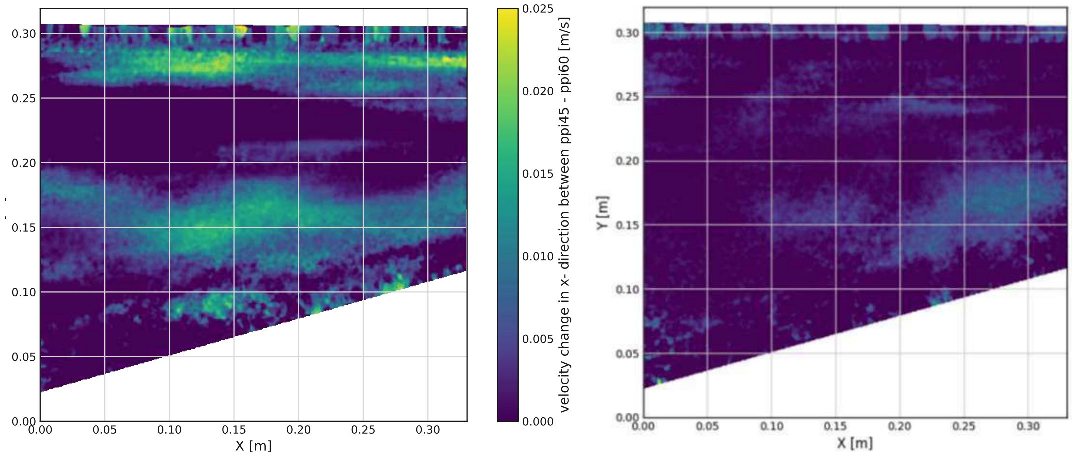


### Position 2: Velocity change between PPI45 and PPI60 in x- direction (right) and y – direction

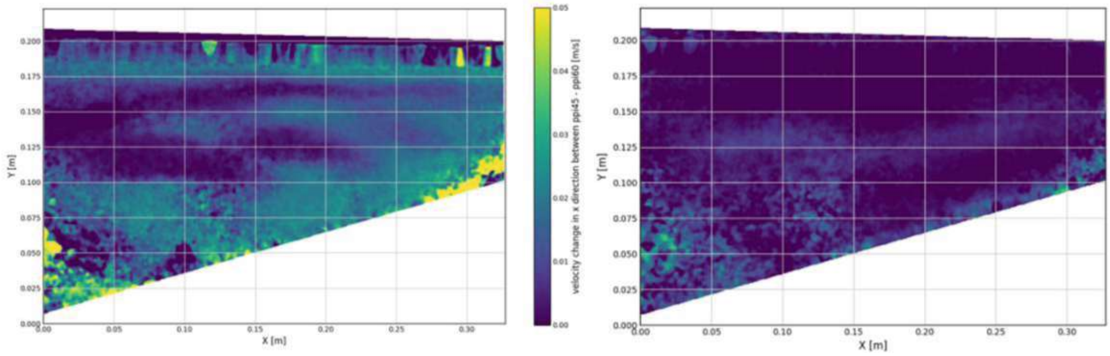


### Position 3: Velocity change between PPI45 and PPI60 in x- direction (right) and y – direction

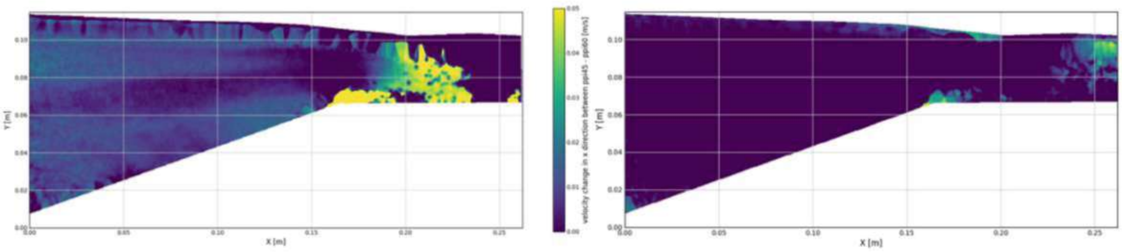

### Position 4: Velocity change between PPI45 and PPI60 in x- direction (right) and y – direction

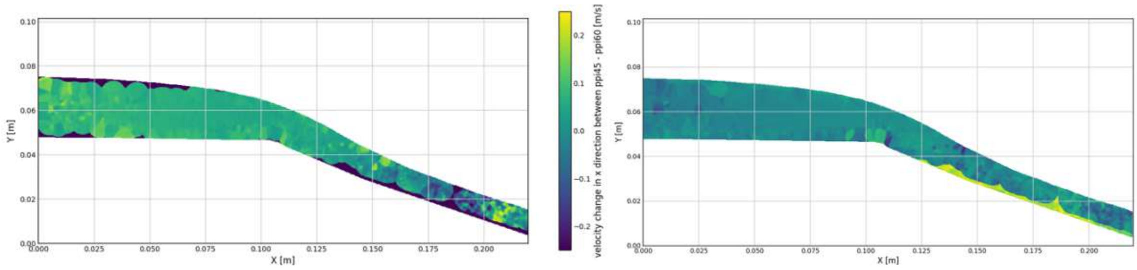


**Position 5: Velocity change between PPI45 and PPI60 in x- direction (right) and y – direction**

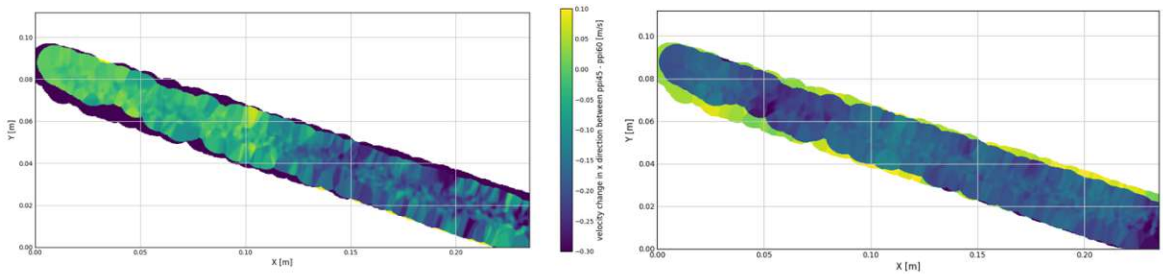


**Position 6: Velocity change between PPI45 and PPI60 in x- direction (right) and y – direction**